

1 **Interpreting U-Pb data from primary and secondary**  
2 **features in lunar zircon**

3

4

5 **M.L. Grange<sup>1\*</sup>, R.T. Pidgeon<sup>1</sup>, A.A. Nemchin<sup>1,2</sup>, N.E. Timms<sup>1</sup>, C. Meyer<sup>3</sup>**

6

7 *<sup>1</sup>Department of Applied Geology, Western Australian School of Mines, Curtin*  
8 *University, GPO Box U1987, Western Australia, 6845, Australia*

9 *<sup>2</sup>Institute für Mineralogie, Münster University, Correnstrasse 24, D-48149, Münster,*  
10 *Germany*

11 *<sup>3</sup>NASA Johnson Space Center, Houston, TX 77058, USA*

12 *\* corresponding author: |e-mail| m.grange@curtin.edu.au; |tel| +61 8 9266 7969*

13

14

## ABSTRACT

15

16

17 In this paper, we describe primary and secondary microstructures and textural  
18 characteristics found in lunar zircon and discuss the relationships between these  
19 features and the zircon U-Pb isotopic systems and the significance of these features  
20 for understanding lunar processes. Lunar zircons can be classified according to: (i)  
21 textural relationships between zircon and surrounding minerals in the host breccias,  
22 (ii) the internal microstructures of the zircon grains as identified by optical  
23 microscopy, cathodoluminescence (CL) imaging and electron backscattered  
24 diffraction (EBSD) mapping and (iii) results of in-situ ion microprobe analyses of the  
25 Th-U-Pb isotopic systems. Primary zircon can occur as part of a cogenetic mineral  
26 assemblage (lithic clast) or as an individual mineral clast and is unzoned, or has sector  
27 and/or oscillatory zoning. The age of primary zircon is obtained when multiple ion  
28 microprobe analyses across the polished surface of the grain give reproducible and  
29 essentially concordant data. A secondary set of microstructures, superimposed on  
30 primary zircon, include localised recrystallised domains, localised amorphous  
31 domains, crystal-plastic deformation, planar deformation features and fractures, and  
32 are associated with impact processes. The first two secondary microstructures often  
33 yield internally consistent and close to concordant U-Pb ages that we interpret as  
34 dating impact events. Others secondary microstructures such as planar deformation  
35 features, crystal-plastic deformation and micro-fractures can provide channels for Pb  
36 diffusion and result in partial resetting of the U-Pb isotopic systems.

37

38 Key Words: lunar zircon – shock features – deformation – U-Pb ages – EBSD –  
39 impact metamorphism

40

41 **1. INTRODUCTION**

42  
43 The first high precision U-Pb measurements on lunar zircon were determined  
44 using the newly developed SHRIMP I (Sensitive High Resolution Ion Micro Probe) at  
45 the Australian National University (Compston et al., 1984). Early results (Meyer et  
46 al., 1985; 1989; 1996) demonstrated that lunar zircons retained their primary U-Pb  
47 ages and that magmatic activity on the Moon lasted from ~4.37 to ~3.90 Ga.  
48 However, complexities in the U-Pb ages and internal structures were found in lunar  
49 zircons by Pidgeon et al. (2007), Nemchin et al. (2009), Grange et al. (2009; 2011)  
50 and Timms et al. (2012), and attributed to disturbance of the U-Pb systems during  
51 impact. The presence of variably isotopically disturbed zircon presents problems in  
52 interpreting U-Pb ages which require distinguishing between primary and secondary  
53 microstructures. In this contribution we describe primary and secondary features in  
54 lunar zircons and link these with the behaviour of the U-Pb system.

55  
56  
57 **2. ANALYTICAL TECHNIQUES**

58  
59 Analytical methods applied to determine the origin of zircon grains in lunar  
60 samples include investigation of (i) spatial relationships between zircon grains and  
61 surrounding minerals using optical microscopy and scanning electron microscopy  
62 (SEM) with secondary and backscattered electron detectors (SE and BSE,  
63 respectively), and energy-dispersive X-ray spectroscopy (EDS); (ii) internal  
64 compositional domains / zoning of zircon grains using BSE and cathodoluminescence  
65 (CL) imaging; (iii) fractures using SE imaging; (iv) quantitative data on  
66 crystallographic orientation using electron backscatter diffraction (EBSD) mapping  
67 that can reveal domains affected by crystal-plastic deformation, containing planar  
68 deformation features, microtwins, and/or fracture-related misorientation; (v)  
69 qualitative and quantitative data on the degree of metamictisation of zircon using  
70 SE/BSE/CL imaging and Raman spectroscopy, respectively; and (vi) in situ U-Pb age  
71 determination using SIMS (Secondary Ion Mass Spectrometry). The analytical  
72 protocols for these techniques are given elsewhere (Williams, 1998; Pidgeon et al.,  
73 2007; Reddy et al., 2007; Timms and Reddy, 2009; Nemchin et al., 2009; Grange et

74 al., 2009). The combination of BSE and EDS has also been used to identify minerals  
75 surrounding zircon grains.

76 Twelve large zircon grains from Apollo 14 and two from Apollo 17 landing  
77 sites showing characteristic internal structures (Table 1) and U-Pb age patterns (Table  
78 2) are described in this study. These grains have been studied using the analytical  
79 protocol described above. All errors for the U-Pb data obtained on individual ion  
80 microprobe spots (Table 2) are shown as 1-sigma, while errors of average, concordia  
81 and intercept ages are given at the 95% confidence level. In addition a set of  
82 previously studied grains is utilised in this discussion for completeness. The full  
83 description of these zircons can be found in Pidgeon et al. (2007), Nemchin et al.  
84 (2009), Grange et al. (2009, 2011) and Timms et al. (2012).

85

86

### 87 **3. CHARACTERISTICS OF LUNAR ZIRCONS AND THEIR U-Pb SYSTEMS**

88

89 Nemchin et al. (2008) proposed a classification of lunar zircons according to  
90 their morphology and recognised a range of morphological types such as euhedral to  
91 rounded zircon grains in breccia matrices and related these features to a relative  
92 history of mechanical abrasion. This classification is useful for answering questions  
93 on the late history of a matrix zircon grain but is not sufficient for addressing more  
94 fundamental questions such as the meaning of zircon U-Pb ages. To provide a basis  
95 for interpreting SIMS U-Pb ages on lunar zircons we have extended the earlier  
96 classification by describing primary and secondary features observed in lunar zircon  
97 grains. We also consider the implications of these features for the interpretation of U-  
98 Pb ages and for deciphering lunar magmatic and impact processes. We use new  
99 analyses of selected grains (Tables 1 and 2) and previous analytical results to illustrate  
100 U-Pb behaviour associated with selected primary or secondary features.

101 To avoid terminological ambiguity, we refer to (i) texture when describing  
102 relationships of the zircon grains with the surrounding minerals (e.g., within a lithic  
103 clast or enclosed in the breccia matrix) and (ii) structure and microstructure of the  
104 zircons when describing internal features of the zircon grains (e.g., zoning, fractures,  
105 etc).

106

107

### 108 3.1. Zircon-rock textural relationships

109

#### 110 3.1.1. Cogenetic zircon in lithic clasts.

111

112 Zircon grains occur as cogenetic mineral phases in lithic clasts and attached to  
113 other mineral(s) representing original rock. In these occurrences, zircon grains can be  
114 relatively large (e.g., 100-800  $\mu\text{m}$  for the ‘pomegranate’ zircon from thin section  
115 73235,82; Pidgeon et al., 2007). In cases where the lithic clast is large or where a  
116 zircon grain is attached to more than one mineral, the composition of the plutonic rock  
117 can be determined from the mineral assemblage. For example, the ‘pomegranate’  
118 zircon (sample 73235,82; Pidgeon et al., 2007) is completely enclosed within an  
119 anorthosite clast and interpreted to have crystallised at the same time as the  
120 anorthosite (Figure 1a-b). The composition of plagioclase ( $\text{An}_{80-85}$ ) indicates that the  
121 clast belongs to the Mg-suite of rocks (Warren and Wasson, 1979), rather than the  
122 ferroan anorthosites. Compston et al. (1984) described a large zircon grain with  
123 truncated zoning and attached to an ilmenite grain. These authors deduced that the  
124 zircon belonged to the population of gabbronorite clasts and crystallised within a  
125 gabbronorite pluton. Another example of zircon grain that is completely enclosed in a  
126 rock fragment is the ‘cracker’ zircon (sample 73235,60#5; Grange et al., 2011; Figure  
127 1c) which is located within a rock fragment described by Meyer et al. (1996) as a  
128 “small granophyric clast of silica and ternary feldspar”, and is interpreted to have  
129 crystallized from a felsic melt. Zircon grains included in lithic clasts usually preserve  
130 their original (often euhedral) shape and also exhibit various degrees of fracturing  
131 (e.g., the ‘cracker’ zircon described above preserves its original prismatic habit).

132

#### 133 3.1.2. Zircon growth in impact melt

134

135 There have been several reports of lunar zircons that have crystallised directly  
136 from impact melt (Gnos et al., 2004; Grange et al., 2009; Liu et al., 2009, 2010,  
137 2012). These grains are relatively small compared to those previously described (<20  
138  $\mu\text{m}$ ) and show distinctive morphological features supporting contemporaneous growth  
139 of zircon in the melt. Poikilitic zircons (i.e., zircon grains enclosing other minerals)  
140 described within the Sayh al Uhaymir 169 (SaU 169) lunar meteorite, have been  
141 interpreted to have formed by crystallisation from small pockets of interstitial impact

142 melt (Gnos et al., 2004; Liu et al., 2009; [Figure 2a](#)). Zircons with similar textures  
143 were described in impact melt breccias collected at the Apollo 12 landing site  
144 (samples 12032 and 12033), and provide further evidence of zircon crystallization  
145 from an impact melt (Liu et al., 2010, 2012). An acicular zircon grain in lunar sample  
146 73217,52 surrounded by felsic glass was also interpreted to have formed during  
147 quenching of an impact melt ([Figure 2b](#)) (Huber and Warren, 2008; Grange et al.,  
148 2009). The unusual shape of this grain, together with the similar shape of surrounding  
149 phases such as ilmenite and K-feldspar ([Figure 2b](#)), indicate that they have formed as  
150 a result of rapid crystallisation in the melt.

151

### 152 3.1.3. Zircon clasts

153

154 Most zircons in lunar breccias occur as individual broken and rounded grains  
155 that have been subjected to a history of impact events prior to incorporation in the  
156 breccia ([Figure 3](#)). Zircon #3 of the aphanitic impact melt breccia 73235,59 ('tiger'  
157 zircon, [Figure 3a](#)) and the 'arrowhead' zircon (sample 76295,91; [Figure 3b](#)), as well  
158 zircon #2 from 14306,60 ([Figure 4h](#)) and the 'teardrop' zircon (zircon #1 from  
159 14083,35, [Figure 4a-b](#)) are large compared to grain size of other rock-forming  
160 minerals that constitute the breccia matrix. The first two zircons have subrounded  
161 grain boundaries, and are anhedral, whereas zircon #2 from 14306,60 ([Figure 4h](#)) and  
162 the 'teardrop' zircon (zircon #1 from 14083,35, [Figure 4a-b](#)) are subhedral. In  
163 addition, many of the studied zircon clasts (with the exception of the 'tiger' zircon)  
164 show oscillatory and/or sector zoning that indicate crystallisation within a magma  
165 chamber or a thick melt sheet ([Figure 4](#)). However, many zircon clasts are small  
166 ([Figure 3c-d](#)) and have irregular and angular or rounded shapes that resulted from  
167 mechanical abrasion and fragmentation during transport in the ejecta. The loss of  
168 physical connection of individual zircon clasts with their igneous source rock, and  
169 modification of their external morphology as a result of abrasion and/or fragmentation  
170 during transport are analogous to detrital zircon grains found in sedimentary rocks on  
171 Earth. Consequently, intragrain microstructures, grain chemistry and the U-Th-Pb  
172 system are the only features of these grains that can be used to interpret their history  
173 prior to fragmentation and incorporation into their host breccia sample

174

## 175 3.2. Zircon microstructures

176

177 Most of the studied lunar zircon grains have primary features indicative of a  
178 magmatic origin and a simple post-crystallisation history. However, several grains  
179 have secondary internal microstructures, geochemical variability and a disturbed U-Pb  
180 system.

181

### 182 3.2.1. Primary zircon microstructures

183

184 *3.2.1.1 Zircon grains with primary zoning.* Oscillatory and sector zoning in terrestrial  
185 zircons are commonly used as an indicator of magmatic crystallisation and the same  
186 applies to zoned lunar zircon grains. Examples of oscillatory zoning in lunar zircons  
187 characterised by multiple, thin, concentric euhedral layers with different  
188 birefringence, BSE and CL properties are shown in [Figure 4a-e](#). Lunar zircons with  
189 sector zoning, where grains comprising several, sometimes irregular, sectors with  
190 sharp boundaries and significant differences in birefringence, BSE and CL properties  
191 are shown in [Figure 4f-h](#). The difference in CL signal intensity, from one thin zone (or  
192 sector) to another commonly correlates with different concentrations of REE, U and  
193 Th. For example, the darkest zone of zircon grain 14306,60#2 ([Figure 4h](#)) has U and  
194 Th concentration of 51 and 32 ppm respectively (analysis 306-60-203, [Table 2](#)),  
195 whereas the bright zone has U and Th content of 13 and 4 ppm (analyses 306-60-201  
196 and -202, [Table 2](#)). Variations in U and Th concentration between sectors contrast  
197 with their narrow range within individual sectors. U-Pb systems of zircons with  
198 internal structures interpreted to have a magmatic origin with no superimposed  
199 secondary microstructures usually show internally reproducible ages from multiple  
200 analyses, suggesting that zircons exhibiting these structures have not experienced any  
201 significant Pb-loss. Consequently, these analyses define the crystallisation age of the  
202 grains in their plutonic setting. This is the case for the ‘teardrop’ zircon (zircon#1 of  
203 14083,35; [Figure 4a-b](#)) that shows both oscillatory (see insert in [Figure 1b](#)) and sector  
204 (white arrow in [Figure 1b](#)) zoning indicative of a magmatic origin: the  $^{207}\text{Pb}/^{206}\text{Pb}$   
205 weighted average of the six analyses ([Table 2](#)) yield an age of  $4040 \pm 3$  Ma (95%  
206 conf., MSWD = 0.47) that is consistent with the intercept age ( $4039 \pm 6$  Ma; [Figure](#)  
207 [5a-b](#)). The U and Th contents of the grain range from 52 to 113 ppm and 35 to 84 ppm  
208 respectively, with Th/U between 0.68 and 0.97. These values demonstrate the  
209 uniformity in age across the grain and a limited variation in U and Th contents ([Table](#)

210 2). This is a typical primary zircon and the consistent age is interpreted as dating the  
211 original crystallisation of the zircon.

212

213 *3.2.1.2. Unzoned grains.* Grains that are completely homogenous and featureless, as  
214 indicated by all available imaging techniques are also interpreted as primary  
215 magmatic zircon (e.g., the ‘hexagon’ zircon, sample 73235,60#4, [Figure 4i-j](#)). These  
216 grains generally have low yet uniform CL intensity, a very limited range of U and Th  
217 concentrations and consistent U-Pb ages. Interpretations of the origin and age from  
218 this type can be ambiguous as there is still a possibility that such grains could have  
219 been completely reset by impact. Nevertheless, in the absence of evidence to the  
220 contrary, zircons showing homogenous internal structures, chemistry and age are  
221 interpreted as dating primary magmatic growth. The ‘hexagon’ grain shows a  
222 homogenous internal structure ([Figure 4i-j](#)) and yields a weighted average  $^{207}\text{Pb}/^{206}\text{Pb}$   
223 age obtained from 6 analyses at  $4364 \pm 5$  Ma (95% conf., MSWD = 1.10, Grange et  
224 al., 2011), which is also similar to the intercept age ( $4364 \pm 5$ Ma; [Figure 5c-d](#)). The U  
225 (100-128 ppm) and Th (57-73 ppm) contents across the grain show very good  
226 consistency and little variation corresponding to Th/U from 0.58 to 0.60 (Grange et  
227 al., 2011).

228

229 *3.2.2. Secondary zircon microstructures*

230

231 *3.2.2.1. Solid state recrystallisation microstructures.* Microstructures that indicate  
232 solid state recrystallisation in terrestrial zircon are characterised by the formation of  
233 intrusive domains of homogeneous bright CL zircon with sharp, irregular boundaries  
234 that truncate primary zoning. The external morphology of a grain is not changed  
235 (Pidgeon 1992; Geisler et al., 2007). Similar relationships are also found in some  
236 lunar zircons. Multiple ion microprobe analyses of low U and secondary patches in  
237 lunar zircon grains are commonly internally consistent and suggest complete resetting  
238 of U-Pb during the event that formed these structures. The ‘tiger’ grain (impact melt  
239 breccia 73235,59; Grange et al., 2011; Timms et al., 2012) contains two small zones  
240 along its border visible in BSE and CL images ([Figures 3a and 6a](#)) that are brighter in  
241 CL and have better quality EBSD patterns. The U-Pb age of these highly crystalline  
242 secondary parts along the edges of the grain are much younger than the bulk part of  
243 the grain (about 250 m.y. younger; [Figure 7a](#); Grange et al., 2011). They also show



244 significantly lower U and Th contents, 19 and 7 ppm respectively, as well as lower  
245 Th/U (0.37) while the rest of the grain has U and Th concentrations above 48 and 24  
246 ppm and Th/U ratios above 0.51 (Grange et al., 2011). This bright CL patch might be  
247 interpreted as a truncated overgrowth but as it actually transgresses the main body of  
248 the grain we interpret it as an area of solid state recrystallisation (secondary zircon).

249

250 *3.2.2.2. Zircon as a product of reaction structures.* In addition to solid state  
251 modification of magmatic zircon, new zircon can form by reaction of other Zr-rich  
252 minerals. An example has been observed in the sample 73217,52 (Figure 6b, Grange  
253 et al., 2009) and shows a corona of microcrystalline zircon around a single  
254 baddeleyite grain. It is interpreted to represent a reaction of baddeleyite with  
255 surrounding silica-rich melt to create new granular zircon. The formation of zircon by  
256 reaction of baddeleyite with melt is summarised by  $\text{ZrO}_2$  (baddeleyite) +  $\text{SiO}_2$  (silica)  
257 =  $\text{ZrSiO}_4$  (zircon). The new zircon has U ranging from 65 to 74 ppm and Th from 46  
258 to 50 ppm, Th/U between 0.64 and 0.79 and a consistent U-Pb age of  $3929 \pm 10$  Ma  
259 which is much younger than the parent baddeleyite age of  $>4275$  Ma (Grange et al.,  
260 2009). The difference in ages indicates that the granular zircon has grown during a  
261 secondary event.

262

263 *3.2.2.3. Structures showing amorphous domains.* The ‘pomegranate’ zircon, first  
264 described by Smith et al. (1986) and studied in detail by Pidgeon et al. (2007) is an  
265 example of localised amorphous domains. The original (primary) zircon preserves  
266 sector zoning in CL (Figure 4f and Figure 8a), characteristic of a magmatic growth,  
267 and has been broken into numerous angular fragments that are bound by a modified  
268 (secondary) zircon that is dark in CL and has low surface relief in SE, high U and Th  
269 contents and no EBSD patterns (Figure 8a-c). Detailed U-Pb analyses of this grain  
270 (Pidgeon et al., 2007) showed that the secondary zircon yields a weighted mean  
271  $^{207}\text{Pb}/^{206}\text{Pb}$  age of  $4187 \pm 11$  Ma (95% conf.), interpreted to be the age of an impact  
272 event. The crystalline fragments give ages approximately 130 m.y. older (Figure 7b)  
273 and have higher Th/U and lower U content than the secondary zircon (Figure 9). The  
274 ‘propeller’ grain (zircon #6 from sample 73215) also has narrow dark CL domains  
275 with similar characteristics as the ‘pomegranate’ zircon (Figure 8d-e). The unmodified  
276 parts of these two grains show high relief in SE images, low U and Th concentrations,  
277 and EBSD patterns with high band contrast indicating that they have retained their

278 crystal integrity. However, the propeller grain is more complex and has also domains  
279 that have undergone crystal-plastic deformation.

280

281 *3.2.2.4. Crystal-plastic deformation.* Many of the studied lunar zircon grains preserve  
282 crystallographic distortions in the form of deformation bands and subgrain  
283 microstructures that are formed by the formation and migration of dislocations, and  
284 can be seen by EBSD mapping. Recent research on terrestrial zircon has shown that  
285 distortion of the lattice by crystal-plasticity facilitate U, Th, REE, Ti and Pb to  
286 migrate through the zircon (Reddy et al., 2006; Timms et al., 2006; Moser et al., 2009,  
287 2011; Timms and Reddy, 2009; Timms et al., 2011). In lunar zircon, this type of  
288 deformation is accompanied by a spread of U-Pb ages along the concordia curve (i.e.,  
289 form a discordia close to the concordia curve) that is taken as evidence of partial  
290 resetting of the U-Pb system. The ‘tiger’ (73235,59#3; [Figure 10a](#)), the ‘oldest’  
291 (72215,195; [Figure 10b](#)), the ‘arrowhead’ (76291,195; [Figure 10c](#)) and the ‘propeller’  
292 (73215,122#6; [Figure 8d](#)) zircon grains preserve crystal-plastic deformation  
293 microstructures leading to various degrees of cumulative misorientation (respectively,  
294 4°, 12°, 15° and 22°; Timms et al., 2012). U-Pb data for these grains show a  
295 continuous spread of ages rather than a single age ([Figure 7a and 11](#); see also  
296 Nemchin et al., 2009, for the oldest zircon). The ‘arrowhead’ grain (sample 76295,91)  
297 has ages between  $4276 \pm 9$  and  $4110 \pm 9$  Ma ([Table 2](#)) and shows a complex  
298 relationship between U-Pb systems and deformations microstructures. The main part  
299 of the ‘propeller’ grain (73215,122#6) also shows a significant range of U-Pb ages,  
300 most likely resulting from different degrees of resetting via fast pathway diffusion  
301 during crystal-plastic deformation ([Figures 6b and 11](#)). If the low-crystalline domains  
302 of the ‘propeller’ zircon (see above; [Figures 8 and 9](#)) formed during a secondary  
303 event, then the two U-Pb ages obtained for the tips of the grain could tentatively be  
304 used to define this event at  $4308 \pm 11$  Ma ([Figure 11](#)). However, there is a possibility  
305 that the youngest age only represents an oldest limit for the age of the secondary  
306 event. Conversely, the oldest analyses may only represent a youngest limit for the age  
307 of igneous crystallisation.

308

309 *3.2.2.5. Discrete planar deformation features (PDFs).* Although lunar zircons have  
310 been subjected to a history of impact events, they only rarely show impact generated  
311 parallel deformation features such as those observed in zircons from terrestrial impact

312 environments (Pidgeon et al., 2011). However, a recent study (Timms et al., 2012)  
313 reported two lunar zircon grains with thin planar features, visible under the optical  
314 microscope, in EBSD mapping and some in CL images. These microstructures  
315 comprise thin (<200 nm) lamellae that occur along a limited number of rational, low  
316 index crystallographic planes, containing either zircon with a high defect density, or  
317 diaplectic glass (Timms et al., 2012). Some PDFs contain microtwin lamellae with a  
318  $65^\circ / \{110\}$  symmetry relationship (Timms et al., 2012). The ‘tiger’ (73235,59#3), the  
319 ‘arrowhead’ (76295,91) and the zircon #62 from the sample 14306,60 have two very  
320 similar sets of planar features visible in cross-polarised light (Figure 12a-c), and to a  
321 lesser extent in plain-polarised light, and also as low EBSD pattern quality features in  
322 EBSD maps (Figures 10c and 12d). Up to five PDFs with different crystallographic  
323 orientations have been recognised in single lunar zircon grain (i.e., ‘tiger’ and  
324 ‘arrowhead’ grains; Timms et al., 2012). However, they are not visible in BSE or CL  
325 images, and do not index as another phase (such as reidite) during the EBSD  
326 acquisition. They cut through both the bright CL domains of the ‘tiger’ grain (formed  
327 by solid state recrystallisation) and the weak plastically deformed main part of the  
328 grain, indicating that they postdate these structures. Zircon grain (14303,49#3) shows  
329 a well-developed set of planar features that are visible in plain- and cross-polarised  
330 light and CL images (Figure 12e). One primary fragment in the ‘pomegranate’ zircon  
331 (73235,82) also shows planar features visible in cross-polarised light (Figures 7 and  
332 8b of Pidgeon et al., 2007). Grains such as the ‘tiger’, the ‘pomegranate’ and the  
333 ‘arrowhead’, are also deformed by dislocation creep and so, PDFs could represent fast  
334 diffusion pathways and channel Pb diffusion through the grain and contribute to the  
335 observed scatter of U-Pb analyses. However, the widths of these microstructures (<5  
336  $\mu\text{m}$ ) are much less than the diameter of typical in situ SIMS pits ( $\sim 20 \mu\text{m}$ ), which  
337 precludes dating them directly.

338

339 *3.2.2.6. Fractures.* Unlike PDFs, fractures in lunar zircons are irregular, do not follow  
340 specific crystallographic orientations and seem to be randomly distributed throughout  
341 the grains (see discussion in Pidgeon et al., 2011). Fragmentation by fracturing can  
342 result in significant relative rotation of individual zircon parts (Figure 13). EBSD  
343 mapping shows that fragments of the ‘cracker’ zircon (73235,60#5) are misoriented  
344 relative to each other (up to  $40^\circ$ ), but none of the fragments are deformed internally.  
345 The individual fragments give similar ages, showing that this structure results only in

346 mechanical damage with no visible chemical or isotopic effect, unless analyses cross  
347 one of the fractures, where contamination is likely. For example, the ‘cracker’ and  
348 zircon #1 from sample 14303,49 show a scatter of U-Pb data along a discordia close  
349 to the concordia curve of 45 m.y. and 90 m.y. respectively (Figure 14a-b). However,  
350 when the analyses representing spots that overlap fractures are removed based on the  
351 after run investigation of spot locations within the grains (Figure 14b-c), remaining  
352 analyses produce internally consistent weighted mean ages of  $4208 \pm 8$  Ma and  $4317$   
353  $\pm 11$  Ma, respectively.

354

355 *3.2.2.7. Radiation damage.* Damage to the crystal lattice is caused by nuclide recoil  
356 and alpha emission during radioactive decay of U and Th. The degree of radiation  
357 damage depends on the total  $\alpha$ -dose received by the zircon, which is a function of the  
358 Th and U content and time. Lunar zircons formed between 4.3 and 3.9 Ga with low  
359 concentrations of radioactive elements (i.e., U and Th contents rarely exceeding 100  
360 ppm; Table 2) will, to the present day, have accumulated an  $\alpha$ -dose between about  
361  $2.5 \times 10^{18}$  and  $3.5 \times 10^{18}$   $\alpha$ -decays/g. This is slightly higher than the first percolation  
362 point defined at  $\sim 3.0 \times 10^{18}$   $\alpha$ -decays/g (Murakami et al., 1991; Salje et al., 1999),  
363 indicating that the radiation damage of these grains have reached the point where  
364 metamict domains are interconnected (i.e., forming opened pathways for diffusion)  
365 only in the last billion year. A 4.3 Ga zircon with average low concentrations of U and  
366 Th will have less than  $0.5 \times 10^{18}$   $\alpha$ -decays/g by 3.9 Ga, suggesting that such zircon has  
367 remained crystalline through the early history of the Moon and that radiation damage  
368 is not a significant factor in the re-setting or disturbance of U-Pb systems of lunar  
369 zircons that have experienced impact events between 4.4 and 3.9 Ga. Only zircons  
370 with an age of  $\sim 4.3$  Ga and concentrations of U in excess of 400-500 ppm and Th  
371 above 200-300 ppm will have accumulated sufficient  $\alpha$ -dose to reach the first  
372 percolation point by 3.9 Ga, and become susceptible to diffusional Pb-loss during  
373 impact metamorphism. The only zircon grains that may have suffered radiation  
374 damage within a relatively short time frame (i.e., a few hundreds of million years) are  
375 zircons from 14321,1613. They have U and Th concentrations (Table 2) that would  
376 have created an alpha dose 10 to 100 times higher than the other zircon grains,  
377 making them more susceptible to Pb loss. These zircons have younger, ages  
378 comprised between 3.97 and 4.00 Ga (Table 2), yet concordant to slightly discordant,

379 indicating that even those grains may not have suffered huge amount of Pb loss before  
380 3.9 Ga.

381

382

383

#### 4. INTERPRETING U-Pb DATA IN LUNAR ZIRCONS

384

##### 4.1. Origin of U-Pb system disturbance in lunar zircon

385

386  
387 Lunar breccias contain a record of multiple impact events which have  
388 repeatedly shocked, pulverised, metamorphosed and mixed materials such that the  
389 largest surviving fragments of igneous rock rarely exceed 1 cm in size and adjacent  
390 apparently identical rock fragments and mineral grains can have different origins and  
391 ages. This introduces serious problems of sample selection for geochronological  
392 methods that analyse composite mineral samples. In addition, the vulnerability of  
393 systems such as Rb-Sr and Ar-Ar to resetting during thermal events associated with  
394 impact metamorphism constrains the ability of these techniques to date events that  
395 occurred before the last major impact. On the other hand our results and earlier studies  
396 (e.g., Meyer et al., 1996) show that the U-Pb system of zircon remains closed under  
397 all but the most extreme lunar impact events giving this system a unique importance  
398 in investigating the early history of the Moon. Another great advantage of zircon  
399 geochronology is that robust U-Pb ages can be determined from a single zircon grain,  
400 and the consistency of the age can be tested by making a number of in situ ion  
401 microprobe U-Pb analyses on different parts of the grain. However, the meaning of  
402 the age is a major question and understanding of the significance of the internal  
403 structures of lunar zircon grains is vital to clarify whether the ages date a primary  
404 igneous event or represent a secondary U-Pb disturbance (complete or partial).

405 Several of these lunar processes are similar to those known to form specific  
406 zircon microstructures and textures on Earth. Consequently, understanding the  
407 formation of these microstructures and textures in lunar zircons can build from the  
408 extensive experience of studying terrestrial rocks. However, evidence for a number of  
409 processes very common on Earth, such as hydrothermal alteration and metamorphism,  
410 especially metamorphism accompanied by the migration of large volumes of fluid has  
411 never been recorded on the Moon. Although water has been detected in some apatite  
412 grains from mare basalts and picritic glass beads (e.g. Saal et al., 2008; Boyce et al.,

413 2010; Hauri et al., 2011) suggesting that the Moon is not completely dry, a total  
414 absence of hydrous minerals such as amphiboles and micas in lunar rocks argues  
415 strongly for very subdued, if not absent, influence of water-rich fluid on the formation  
416 of lunar rocks. As a result several features present in lunar zircon that resemble those  
417 observed in terrestrial zircons are interpreted to form by different processes. In  
418 particular hydrothermal processes and metamorphism have to be excluded from  
419 consideration when explaining textures and microstructures of lunar zircons.  
420 Magmatism and impacts appear to be the only major processes that can be invoked to  
421 interpret these textures and microstructures.

422

#### 423 **4.2. U-Pb in zircon with primary microstructures**

424

425 One of the microstructures common in magmatic zircon on Earth is sector  
426 zoning. It is also common in lunar zircons (Figure 4f-h) and is interpreted as primary  
427 igneous feature. The consistency and concordance of SIMS U-Pb ages on different  
428 sectors in such grains is strong evidence that the age represents primary crystallisation  
429 (Figure 15a). On the other hand, oscillatory zoning is rare in zircons from lunar  
430 breccias. The poor representation of oscillatory zoning in lunar zircon is a striking  
431 feature and could be taken as an additional indication of absence of water in lunar  
432 magmas, resulting in significantly higher solidus temperature, lower degree of  
433 polymerisation and lower viscosity of these melts, which makes diffusion of trace  
434 elements (such as REE) within the magma more efficient. Formation of oscillatory  
435 zoning is possibly determined by the relative rates of supply of trace elements to the  
436 growing zircon interface (Mattinson et al., 1996). Faster diffusion will, therefore, be  
437 expected to reduce the probability of development of inhomogeneities such as  
438 oscillatory zoning in the zircon grains and favour the development of homogeneous  
439 grains. Vavra (1990) interpreted the different patterns of zoning as reflecting different  
440 conditions of zircon saturation (high for oscillatory zoning and low for sector zoning)  
441 of the melt and linked growth zoning with growth kinematics. It is therefore likely  
442 that the zoning of the lunar zircon is associated with the chemical composition of the  
443 melt and its liquidus temperature. Notwithstanding the reasons for scarcity of  
444 oscillatory zoned zircons in lunar rocks, when this microstructure is present, the  
445 grains can be viewed as formed by crystallisation from magma and their ages  
446 representing magmatic crystallisation.

447 One group of zircon grains which is usually difficult to interpret in both  
448 terrestrial and lunar rocks are those without any internal structures as revealed by  
449 cathodoluminescence (e.g., [Figure 4i](#)). In rocks on Earth these grains can be formed  
450 by both magmatic and metamorphic processes. Lunar grains found as fragments in the  
451 breccia matrixes can be interpreted as crystallising from a magma or representing a  
452 complete recrystallization and resetting of U-Pb system during impacts. However,  
453 where ion microprobe U-Pb ages over the polished surface of such unzoned grains are  
454 consistent and concordant we tentatively interpret the ages as dating igneous  
455 crystallisation.

456

### 457 **4.3. U-Pb in zircon grown from the impact melt**

458

459 The presence of zircon grains in quenched and poikilitic impact melts ([Figure](#)  
460 [2](#)) offers a useful opportunity to unequivocally date an impact event ([Figure 15b](#)). In  
461 addition, the habits of these grains also provide information on viscosity and melt  
462 polymerisation. The small zircon grains from the SaU 169 meteorite and from Apollo  
463 12 breccia samples are intergrown with other minerals in poikilitic melts, whereas the  
464 zircon growing in the melt from 73217,52 sample is acicular, almost dendritic. These  
465 habits indicate rapid crystallisation in an impact melt and consistent ion microprobe  
466 ages on such grains are reliably interpreted as dating the impact. Differences in the  
467 texture of these impact melt zircons are likely to be the result of contrasting chemical  
468 composition of the impact melts, mafic in the SaU 169 and Apollo 12 samples and  
469 silica-rich, high-K in the sample 73217,52. It is also likely that these differences in  
470 chemistry are linked to the saturation and temperature of crystallisation of the zircon.  
471 It is worth noting that the impact origin of the melt in 73217,52 has been subject of  
472 controversy (for full discussion and references see Grange et al., 2009). Nevertheless,  
473 the acicular shape of zircon leaves little doubt that it could only form in this melt and  
474 therefore dates the time of its quenching, interpreted to be caused by an impact (Huber  
475 and Warren, 2008).

476

### 477 **4.4. U-Pb data in zircon with secondary microstructures**

478

479 Whereas undisturbed primary structures in lunar zircons described above have  
480 petrological significance, the consistency of ion microprobe U-Pb ages throughout the



481 grain is an essential criterion for interpreting the age as a primary age. As  
482 demonstrated in this contribution and previous studies (e.g. Pidgeon et al., 2007), U-  
483 Pb ages within primary lunar zircons can be severely disturbed by secondary  
484 processes. Generally such disturbances are accompanied by the development of  
485 secondary structures. Some of these structures are well known in zircons from  
486 terrestrial impacts making their interpretation in lunar zircons relatively  
487 straightforward. However, some microstructures observed in impactites on Earth are  
488 rare in zircons from the Moon. For example, the high pressure zircon polymorph  
489 (reidite) has never been found in lunar impact samples. Other impact deformation  
490 structures such as planar deformations features, micro-twins and crystal-plastic  
491 deformation have only been recently found in lunar zircon (Grange et al., 2011;  
492 Timms et al., 2012; [Figures 10 and 12](#)). Many of these microstructures, such as PDFs  
493 cannot be targeted for in-situ U-Pb analyses due to their small size and therefore  
494 cannot be used to determine the age of an impact. However, they could provide fast  
495 diffusion pathways for Pb which can lead to scatter in the U-Pb ages. Therefore, it is  
496 important to recognise such features and be aware of their potential effects on the U-  
497 Pb system ([Figure 15c](#)). In addition, the occurrence of planar microstructures is related  
498 to the shock pressure and temperature experienced by the sample at the time of impact  
499 and can give some insight into conditions attained by the sample during shock  
500 metamorphism and enable recognition of multiple impact events (Timms et al., 2012).

501

#### 502 4.4.1. Reaction products

503

504 As mentioned before, several microstructures identified in lunar zircons  
505 resemble those formed in terrestrial rocks by processes that do not exist on the Moon.  
506 One of these is the growth of zircon around a baddeleyite core which has been  
507 described in terrestrial mafic rocks by Davidson and van Breeman (1988) and  
508 Heaman and LeCheminant (1993) who reported formation of zircon coronas around  
509 baddeleyite as a result of increased silica activity during metamorphism. As  
510 conditions for regional metamorphism do not exist on the Moon, formation of zircon  
511 coronas around baddeleyite in lunar samples can only be explained by (i) reaction of  
512 silica-rich melt with baddeleyite or (ii) solid state reaction between silica-rich glass  
513 and baddeleyite. The single published example of this reaction (Grange et al., 2009;  
514 [Figure 6b](#)) is complicated as the silica melt reacting with the baddeleyite, is



515 significantly older (~ 4.3 Ga, as dated by the acicular zircon growing in the melt) than  
516 the granular zircon in the corona (~3.9 Ga). Solid state reaction is unlikely as  
517 baddeleyite will probably react as soon as it gets in contact with the silica saturated  
518 melt. Thus, the age difference can be explained by either remelting of the silica glass  
519 or complete Pb loss from the granular zircon during a later (~3.9 Ga) event. Both  
520 mechanisms require a secondary thermal pulse at about 3.9 Ga, likely to be associated  
521 with an impact event.

522

#### 523 4.4.2. Recrystallisation and amorphisation

524

525 An important observation described in this report is the recognition of two  
526 contrasting types of secondary microstructures in a number of grains, namely solid  
527 state recrystallisation and amorphisation. These microstructures are particularly  
528 important because they involved resetting of U-Pb system and can form domains and  
529 patches large enough to be dated, and therefore, provide information about the timing  
530 of secondary events (Figure 15d). Recrystallised domains in terrestrial zircons are  
531 often formed as a result of metamorphic reaction involving fluid and possibly melt.  
532 Also, inherited zircon grains can react with a melt nearly saturated in Zr, be partially  
533 dissolved and re-crystallise as new zircon forming distinct rims around inherited  
534 cores. However, mafic nature of lunar melts would require significant degrees  
535 (Dickinson and Hess, 1982) of crystallisation before Zr saturation is reached even if  
536 the starting melt is enriched in incompatible elements, which will probably result in a  
537 complete dissolution of any potential inherited zircon. Consequently, common  
538 processes occurring on Earth cannot explain lunar zircon recrystallised domains  
539 (Figure 6a) that are likely to be formed as a result of impacts, their U-Pb ages  
540 reflecting the timing of these impacts. Amorphous domains in terrestrial grains reflect  
541 initial variability of radioactive elements in the grains and therefore follow specific  
542 pattern consistent with the zircon zoning. Two main features make non-planar  
543 amorphous domains in lunar zircon different from their terrestrial counterparts. First,  
544 their irregular distribution is inconsistent with the primary trace elements variations in  
545 zircon. Second there is a relatively short time between primary and secondary events,  
546 which mean that the lunar zircon is crystalline at the time of disturbance.  
547 Consequently, process other than radiation damage appears to be responsible for the  
548 formation of amorphous zircon domains. The process is likely to be propagation of

549 shock during impact, which can explain the formation of irregular diaplectic glass  
550 domains, especially on the interfaces between different mineral phases, accompanied  
551 by chemical modification and re-setting of the U-Pb system.

552 Although the formation of both re-crystallised and amorphous zircon is  
553 accompanied by complete resetting of the U-Pb system, the modifications of the  
554 zircon lattice and chemistry associated with these microstructures are very different  
555 and provide evidence of two basically different sets of impact conditions. They may  
556 represent formation during different stages of an impact event (Timms et al., 2012).  
557 The ‘tiger’ grain (73235,59#3; [Figure 6a](#)) shows a recrystallised zone, characterised  
558 by a sharp difference in age ([Figure 7a](#)), a sharp decrease in U content and Th/U ratio  
559 compared to the rest of the grain. This can be explained by recrystallisation of the  
560 lattice with concurrent removal of impurities during an impact. In contrast, the  
561 ‘propeller’ (73215,122#6) and the ‘pomegranate’ (73235,82) zircons contain areas  
562 that experienced a significant loss of crystallinity, by shock induced amorphisation,  
563 accompanied by an increase of U concentration and decreasing Th/U ([Figures 8 and](#)  
564 [9](#)). The two contrasting processes of amorphisation and recrystallisation represent a  
565 3D modification of zircon grains and reflect different stages of compression during an  
566 impact. The initial compression shock wave is believed to be accompanied, in a 3D  
567 poly-mineralic rock, by inhomogeneous shock pressures at the grain scale, resulting in  
568 a heterogeneous distribution of shock microstructures, especially localised at the  
569 grains interfaces and near the cracks and pores (e.g., Sharp and DeCarli, 2006).  
570 However, this inhomogeneity exists only for the first fractions of millisecond and the  
571 destructive shock wave quickly decays into seismic (elastic) waves (e.g., Sharp and  
572 DeCarli, 2006). The effect on the crystalline zircon lattice of severe shock is not well  
573 understood, however, experimental results of Gucsik et al. (2002, 2004) suggest that  
574 severe shock can result in damage to the zircon lattice similar to that caused by  
575 radiation. It is therefore possible that shock created a randomly distributed network of  
576 amorphous domains (diaplectic glass) surrounding fragments of highly crystalline  
577 zircon in the ‘pomegranate’ grain. These amorphous domains completely lack any  
578 other overprinting microstructures. The recovery properties of shock induced  
579 amorphisation are not known, however, by analogy with radiation damage, it is  
580 suspected that annealing could occur during a subsequent thermal pulse. Pidgeon et al.  
581 (2007) envisaged the secondary zircon of the ‘pomegranate’ grain to be localised in  
582 the areas of pressure release after the combined shock fracturing and friction heating

583 induced by an impact. This was accompanied by complete Pb-loss during the transient  
584 high temperature conditions during the impact event, locally resetting the U-Pb  
585 system, and therefore the age given by the secondary zircon defines the age of the  
586 impact.

587

#### 588 4.4.3. Fractures

589

590 The formation of any type of fracture in zircon (Figures 13 and 14) introduces  
591 fast pathways for trace element and isotope exchange between the grain and external  
592 environment. For purely brittle fractures, geochemical modification occurs via volume  
593 diffusion from the fracture interface only, over length scales that would depend on the  
594 temperature-time history and diffusivity of the trace element (Figure 15e). The  
595 process of brittle fracture could potentially be coupled with crystal-plastic strain at  
596 some conditions, especially at crack tips. Given that crystal-plasticity of terrestrial  
597 zircon is accompanied by enhanced, heterogeneous diffusion of trace elements,  
598 including U and Th (Timms et al., 2006; Reddy et al., 2007; Timms et al., 2011,  
599 2012), it is important to fully characterise the nature of fractures in lunar zircon. The  
600 studied grains neither show evidence of coupled brittle-ductile process for the  
601 formation of fractures, nor any measurable variations in the U-Pb ages adjacent to the  
602 fractures.

603

#### 604 4.4.4 PDFs and micro-twins

605

606 PDFs and micro-twins are potential pathways for fast diffusion that facilitate  
607 alteration, trace element mobility and Pb-loss during impact or subsequent processes.  
608 For example, PDFs in shocked terrestrial quartz can be decorated by fluid inclusions  
609 that have exsolved during the alteration of diaplectic glass (e.g., Leroux and Doukhan  
610 1996, Grieve et al. 1996). Even if complete resetting occurs along PDFs and micro-  
611 twins, these features are too narrow (typically <1 µm; Figure 12) to be analysed in situ  
612 with ion microprobe. In some terrestrial cases, entire populations of shocked zircon  
613 containing PDF and micro-twin shock features preserve the host rock ages with no  
614 impact-related Pb-loss (Deutsch and Schärer, 1990; Cavosie et al., 2010; Moser et al.,  
615 2011). In other terrestrial examples, zircon with PDFs and granular textures can be  
616 highly discordant, and intercept ages from discordant, incompletely reset grains have

617 been used to infer impact ages (Krogh et al., 1993a,b; Deloule et al., 2001). However,  
618 the precise role of PDFs and micro-twins on the U-Pb system in lunar zircon is  
619 difficult to evaluate with the currently available techniques.

620

#### 621 4.4.4. Dislocation creep

622

623 Crystal-plasticity by dislocation creep introduces fast diffusion pathways that  
624 can permit partial or complete resetting of the U-Pb system in zircon at modest  
625 pressure-temperature conditions in terrestrial rocks (Reddy et al., 2006, 2007; Timms  
626 et al., 2006, 2011, 2012; Moser et al., 2009; [Figure 15f](#)). Available data suggests that  
627 U, Th and Pb are mobilised during deformation along dislocations and low-angle  
628 boundaries, with little post-deformation modification (Timms et al., 2006, 2011).  
629 Therefore, the timing of crystal-plastic deformation is likely to be preserved where  
630 complete resetting of the U-Pb system is achieved. Nemchin et al. (2009) showed that  
631 U-Pb resetting can be heterogeneous at the scale of a single zircon grain, and  
632 demonstrated a correlation between the extent of U-Pb resetting and local lattice  
633 misorientation ('oldest' grain 72215,195; [Figure 10b](#)). The resulting mean age of  $4333$   
634  $\pm 7$  Ma for the most deformed and reset domains is interpreted to represent the age of  
635 a lunar impact event. Other studied crystal-plastically deformed lunar zircon grains  
636 also record a spread of ages, indicating variable degrees of resetting of the U-Pb  
637 system within each grain ([Figures 10 and 11](#)). However, the precision of individual  
638 analysis and the sub-parallel distribution close to concordia precludes using lower  
639 intercept ages to determine an impact age for these grains with confidence.  
640 Nevertheless, in situ U-Pb analysis of crystal-plastically deformed zircon could be a  
641 useful approach to resolve lunar impact ages in scenarios where the impact occurred  
642 significantly later than the initial zircon crystallisation age, as demonstrated for  
643 terrestrial impacts (Moser et al., 2009; 2011), and/or if the precision of in situ  
644 analytical techniques could be improved.

645

646

## 647 5. SUMMARY AND CONCLUSIONS

648

649 In this report we demonstrate the importance of microstructures in lunar  
650 zircons for the interpretation of U-Pb ages and for providing information on the nature

651 of lunar processes. Where zircons have secondary microstructures like amorphisation  
652 or recrystallisation overprinting primary structures, it is possible to obtain the age of  
653 both primary zircon and secondary impact event within the same grain. Where zircons  
654 are individual clasts in the breccia matrix, identification of internal microstructures is  
655 vital in targeting areas for ion microprobe analyses and is necessary for interpreting  
656 the significance of the U-Pb data. The recognition of zircon internal microstructures  
657 has a growing role in providing basic information on lunar processes such as  
658 conditions during magmatic crystallisation and impact. Specific conclusions are:

659 1) Consistent U-Pb ion microprobe ages obtained on isotopically homogenous  
660 lunar zircon grains with igneous internal microstructures (e.g., sector and/or  
661 oscillatory zoning) can be interpreted as magmatic crystallisation ages (primary ages);

662 2) Impact ages can be obtained with a high degree of confidence (i) where  
663 there is evidence zircon has grown within the impact melt (acicular habits or poikilitic  
664 textures) or (ii) where lunar zircons show either recrystallised zones or domains that  
665 have lost their crystallinity. In these last cases, multiple analyses of different textural  
666 domains in the zircons help to better constrain the precise timing of both magmatic  
667 and impact events;

668 3) Some microstructures, including fractures, planar deformation features and  
669 crystal-plastic deformation can facilitate diffusion of Pb, and therefore their  
670 identification should prompt a careful examination of the U-Pb ages and their  
671 significance;

672 4) Secondary zircon formed by (i) recrystallisation has a lower U and lower  
673 Th/U and (ii) amorphisation has a higher U associated with lower Th/U, than the  
674 primary zircon. Mechanisms responsible for these observations are yet to be  
675 determined.

676

677 **Acknowledgements**

678 We thank NASA, and especially the crew of Apollo 14 and Apollo 17 for the  
679 provision of the samples. We are also grateful to E. Gnos who provides us with image  
680 of zircon grain from the meteorite SaU169. MG and NT acknowledge funding from a  
681 Curtin Internal Research Grant. AN and MG acknowledge ARC Discovery Project  
682 DP120102457. Rob Hart is thanked for his assistance with scanning electron  
683 microscopy. Thanks to AE, reviewers Corfu, Cavosie and Moser (anonymous?)  
684

## REFERENCES

- 685  
686 Boyce J.W., Liu Y., Rossman G.R., Guan Y., Eiler J.M., Stolper E.M. and Taylor  
687 L.A. (2010) Lunar apatite with terrestrial volatile abundances. *Nature* **466**, 22  
688 July 2010, 466–469.
- 689 Cavosie A.J., Quintero R.R., Radovan H.A. and Moser D.E. (2010) A record of  
690 ancient cataclysm in modern sand: Shock microstructures in detrital minerals  
691 from the Vaal River, Vredefort Dome, South Africa. *GSA Bulletin* 122(11/12),  
692 1968–1980.
- 693 Compston W., Williams I.S. and Meyer C. (1984) U-Pb geochronology of zircons  
694 from Lunar Breccia 73217 using a sensitive high mass-resolution ion  
695 microprobe. Proceedings of the Lunar and Planetary Science Conference 14th,  
696 *Journal of Geophysical Research* **89**, B525–B534.
- 697 Davidson A. and van Breeman O. (1988) Baddeleyite-zircon relationships in coronitic  
698 metagabbro, Grenville Province, Ontario: implications for geochronology.  
699 *Contributions to Mineralogy and Petrology* **100**, 291–299.
- 700 Deloule E., Chaussidon M., Glass B.P., Koeberl C. (2001) U-Pb isotopic study of  
701 relict zircon inclusions recovered from Muong Nong-type tektites. *Geochimica*  
702 *et Cosmochimica Acta* **65**(11), 1833–1838.
- 703 Deutsch A. and Schärer U. (1990) Isotope systematics and shock-wave  
704 metamorphism: I. U-Pb in zircon, titanite and monazite, shocked experimentally  
705 up to 59 GPa. *Geochimica et Cosmochimica Acta* **54**(12), 3427–3434.
- 706 Dickinson J.E. and Hess P.C. (1982) Zircon saturation in lunar basalts and granites.  
707 *Earth and Planetary Science Letters* **57**(2), 336–344.
- 708 Geisler T., Schaltegger U. and Tomaschek F. (2007) Re-equilibration of zircon in  
709 aqueous fluids and melts. *Elements* **3**, 43–50.
- 710 Gnos E., Hofmann B.A., Al-Katgiri A., Lorenzetti S., Eugster O., Whitehouse M.J.,  
711 Villa I.M., Jull A.J.T., Eikenberg, J., Spettel, B., Krähenbühl U., Franchi I.A.  
712 and Greenwood R.C. (2004) Pinpointing the source of a lunar meteorite:  
713 Implications for the evolution of the Moon. *Science* **305**, 657–659.
- 714 Grange M.L., Nemchin A.A., Pidgeon R.T., Timms N., Muhling J.R. and Kennedy  
715 A.K. (2009) Thermal history recorded by the Apollo 17 impact melt breccia  
716 73217. *Geochimica et Cosmochimica Acta* **73**, 3093–3107.
- 717 Grange M.L., Nemchin A.A., Timms N., Pidgeon R.T. and Meyer C. (2011) Complex  
718 magmatic and impact history prior to 4.1 Ga recorded in zircon from Apollo 17

719 South Massif aphanitic breccia 73235. *Geochimica et Cosmochimica Acta* **75**,  
720 2213–2232.

721 Grieve R.A.F., Langenhorst F. and Stoeffler D. (1996) Shock metamorphism of quartz  
722 in nature and experiment; II, Significance in geoscience. *Meteoritics* **31**(1), 6–  
723 35.

724 Gucsik A., Koerberl C., Brandstätter F., Reimold W.U. and Libowitzky E. (2002)  
725 Cathodoluminescence, electron microscopy, and Raman spectroscopy of  
726 experimentally shock-metamorphosed zircon. *Earth and Planetary Science*  
727 *Letters* **202**, 495–509.

728 Gucsik A., Zhang M., Koeberl C., Salje E.K.H., Redfern S.A.T. and Pruneda J.M.  
729 (2004) Infrared and Raman spectra of ZrSiO<sub>4</sub> experimentally shocked at high  
730 pressures. *Mineralogical Magazine* **68**, 801–811.

731 Krogh T.E., Kamo S.L. and Bohor B.F. (1993a) Fingerprinting the K/T impact site  
732 and determining the time of impact by UPb dating of single shocked zircons  
733 from distal ejecta. *Earth and Planetary Science Letters* **119**(3), 425–429.

734 Krogh T.E., Kamo S.L., Sharpton V.L., Marin L.E. and Hildebrands A.R. (1993b) U-  
735 Pb ages of single shocked zircons linking distal K/T ejecta to the Chicxulub  
736 crater. *Nature* **366**(6457), 731–734.

737 Hauri E.H., Weinreich T., Saal A.E., Rutherford M.C. and Van Orman J.A. (2011)  
738 High pre-eruptive water contents preserved in lunar melt inclusions. *Science*  
739 **333**, 213–215.

740 Heaman L.M. and LeCheminant A.N. (1993) Paragenesis and U-Pb systematics of  
741 baddeleyite (ZrO<sub>2</sub>). *Chemical Geology* **110**, 95–126.

742 Huber H. and Warren P.H. (2008) Enigmatic, largely granitic 73217: A lunar mixed  
743 melt-breccia, but is it impact melt? *Lunar Planetary Science Conference XXXIX*,  
744 Houston, USA, Abstract #2405.

745 Leroux H. and Doukhan J.-C. (1996) A transmission electron microscope study of  
746 shocked quartz from the Manson impact structure. *Geological Society of*  
747 *America Special Paper* **302**, 267–274.

748 Liu D., Wan Y., Zhang Y., Dong C., Jolliff B.L., Zeigler R.A. and Korotev R.L.  
749 (2009) Age of the zircons in the impact-melt breccia in SAU169 lunar  
750 meteorite: Beijing SHRIMP II study. *40th Lunar and Planetary Science*  
751 *Conference*, The Woodlands, USA, Abstract #2499.



752 Liu D., Jolliff B.L., Zeigler R.A., Wan Y., Zhang Y., Dong C. and Korotev R.L.  
753 (2010) A 3.91 billion year age for Apollo 12 high-thorium impact melt breccias:  
754 products of Imbrium, or an older impact basin in the Procellarum KREEP  
755 Terrane? *41th Lunar and Planetary Science Conference*, The Woodlands, USA,  
756 Abstract #2477.

757 Liu D., Jolliff B.L., Zeigler R.A., Korotev R.L., Wan Y., Xie H., Zhang Y., Dong C.,  
758 Wang W. (2012) Comparative zircon U–Pb geochronology of impact melt  
759 breccias from Apollo 12 and lunar meteorite SaU 169, and implications for the  
760 age of the Imbrium impact. *Earth and Planetary Science Letters* **319-320**, 277–  
761 286.

762 Ludwig K.R. (2008) User’s Manual for Isoplot 3.60, A geochronological toolkit for  
763 Microsoft Excel. Berkeley Geochronological Center Special Publication no 4,  
764 revision of 8 April 2008, 77 pp.

765 Mattinson J.M., Graubard C.M., Parkinson D.L. and McLelland W.C. (1996) U-Pb  
766 reverse discordance in zircons: the role of fine-scale oscillatory zoning and sub-  
767 microscopic transport of Pb. American Geophysical Union, *Geophysics*  
768 *Monographs* **95**, 355–370.

769 Meyer C., Compston W. and Williams I.S. (1985) Lunar zircon and the closure age of  
770 the lunar crust. *Lunar Planetary Science Conference 16th*, Houston, USA, 557–  
771 558 (Abstract).

772 Meyer C., Williams I.S. and Compston W. (1989)  $^{207}\text{Pb}/^{206}\text{Pb}$  ages of zircon-  
773 containing rock fragments indicate continuous magmatism in the lunar crust  
774 from 4350 to 3900 million years. *Lunar Planetary Science Conference XXth*,  
775 Houston, USA, 691–692 (Abstract).

776 Meyer C., Williams I.S. and Compston W. (1996) Uranium-lead ages for lunar  
777 zircons: Evidence for a prolonged period of granophyre formation from 4.32 to  
778 3.88 Ga. *Meteoritics & Planetary Science* **31**, 370–387.

779 Moser D.E., Davis W.J., Reddy S.M., Flemming R.L. and Hart R.J. (2009) Zircon U-  
780 Pb strain chronometry reveals deep impact-triggered flow. *Earth and Planetary*  
781 *Science Letters* **277**(1-2), 73–79.

782 Moser D.E., Cupelli C.L., Barker I., Flowers R.M., Bowman J.R., Wooden J. and Hart  
783 R. (2011) New shock phenomena for dating and reconstruction of large impact  
784 basins revealed by zircon microstructural (EBSD, CL), U-Pb and (U-Th)/He

785 analysis of the Vredefort dome. *Canadian Journal of Earth Sciences* **48**, 117–  
786 139.

787 Murakami T., Chakoumakos B.C., Ewing R.C., Lumpkin G.R. and Weber W.J.  
788 (1991) Alpha-decay event damage in zircon. *American Mineralogist* **76**, 1510–  
789 1532.

790 Nemchin A.A., Pidgeon R.T., Whitehouse M.J., Vaughan J.P. and Meyer C. (2008)  
791 SIMS U-Pb study of zircon from Apollo 14 and 17 breccias: Implications for  
792 the evolution of lunar KREEP. *Geochimica et Cosmochimica Acta* **72**, 668–689.

793 Nemchin A., Timms N., Pidgeon R., Geisler T., Reddy S. and Meyer C. (2009)  
794 Timing of crystallisation of the lunar magma ocean constrained by the oldest  
795 zircon. *Nature Geoscience* **2**(2), 133–136.

796 Pidgeon R.T. (1992) Recrystallisation of oscillatory zoned zircon: some  
797 geochronological and petrological implications. *Contributions to Mineralogy  
798 and Petrology* **110**, 463–472.

799 Pidgeon R.T., Nemchin A.A., van Bronswijk W., Geisler T., Meyer C., Compston W.  
800 and Williams I.S. (2007) Complex history of a zircon aggregate from lunar  
801 breccia 73235. *Geochimica et Cosmochimica Acta* **71**, 1370–1381.

802 Pidgeon R.T., Nemchin A.A. and Kamo S.L. (2011) Comparison of structures in  
803 zircons from lunar and terrestrial impactites. *Canadian Journal of Earth  
804 Sciences* **48**, 107–116.

805 Prior D.J., Boyle A.P., Brenker F., Cheadle M.C., Day A., Lopez G., Peruzzo L., Potts  
806 G.J., Reddy S., Spiess R., Timms N.E., Trimby P., Wheeler J. and Zetterström  
807 L. (1999) The application of electron backscatter diffraction and orientation  
808 contrast imaging in the SEM to textural problems in rocks. *American  
809 Mineralogist* **84**, 1741–1759.

810 Reddy S.M., Timms N.E., Trimby P., Kinny P.D., Buchan C. and Blake K. (2006)  
811 Crystal-plastic deformation of zircon: A defect in the assumption of chemical  
812 robustness. *Geology* **34**, 257–260.

813 Reddy S.M., Timms N.E., Pantleon W. and Trimby T. (2007) Quantitative  
814 characterization of plastic deformation of zircon and geological implications.  
815 *Contributions to Mineralogy and Petrology* **153**, 625–645.

816 Saal A.E., Hauri E.H., Cascio M.L., Van Orman J.A., Rutherford M.C. and Cooper  
817 R.F. (2008) Volatile content of lunar volcanic glasses and the presence of water  
818 in the Moon's interior. *Nature* **454**, 10 July 2008, 192–195.

819 Salje, E.K.H., Chrosch J. and Ewing R.C. (1999) Is “metamictization” of zircon a  
820 phase transition? *American Mineralogist* **84**, 1107–1116.

821 Sharp T.G. and DeCarli P.S. (2006) Shock effects in meteorites. In *Meteorites and the*  
822 *Early Solar System II* (eds. D.S. Lauretta, H.Y. McSween), University of  
823 Arizona Press, pp. 653–677.

824 Smith J.M., Meyer C., Compston W. and Williams I.S. (1986) 73235,82  
825 (pomegranate): an assemblage of lunar zircon with unique overgrowth. *17th*  
826 *Lunar and Planetary Science Conference*, Houston, 805–806 (Abstract).

827 Stacey J.S. and Kramers J.D. (1975) Approximation of terrestrial lead isotope  
828 evolution by a two-stage model. *Earth and Planetary Science Letters* **26**, 207–  
829 221.

830 Timms N.E. and Reddy S.M. (2009) Response of cathodoluminescence to crystal-  
831 plastic deformation in zircon. *Chemical Geology* **261**, 12–24.

832 Timms N.E., Kinny P.D. and Reddy S.M. (2006) Enhanced diffusion of Uranium and  
833 Thorium linked to crystal plasticity in zircon. *Geochemical Transactions* **7**(10),  
834 1–16.

835 Timms N.E., Kinny P.D., Reddy S.M., Evans K., Clark C. and Healy D. (2011)  
836 Relationship among titanium, rare earth elements, U–Pb ages and deformation  
837 microstructures in zircon: Implications for Ti-in-zircon thermometry. *Chemical*  
838 *Geology* **280**, 33–46.

839 Timms N.E., Reddy S.M., Healy D. Nemchin A.A., Grange M.L., Pidgeon R.T., Hart  
840 R. (2012) Resolution of impact-related microstructures in lunar zircon: A shock-  
841 deformation mechanism map. *Meteoritics and Planetary Science* **47**(1), 120–  
842 141.

843 Vavra G. (1990) On the kinematics of zircon growth and its petrogenetic significance:  
844 a cathodoluminescence study. *Contributions to Mineralogy and Petrology* **106**,  
845 90–99.

846 Warren P.H. and Wasson J.T. (1979) The compositional-petrographic search for  
847 pristine nonmare rocks - Third foray. *Proceedings 10th Lunar and Planetary*  
848 *Science Conference* **1**, 583–610.

849 Williams I.S. (1998) U-Th-Pb geochronology by ion microprobe. In *Applications of*  
850 *microanalytical techniques to understanding mineralising processes* (eds. M.A.  
851 McKibben, W.C. Shanks, W.I. Riley), *Reviews in Economic Geology* **7**, 1–35.

852

## LIST OF TABLES

853

854

855 [Table 1](#) – Summarised description of new zircon grains.

856

857 [Table 2](#) – Ion microprobe U-Pb results of new zircon grains.

858

859

860

## FIGURE CAPTIONS

861

862

### 863 **Figure 1 – Zircon enclosed into lithic clast**

864 (a) ‘Pomegranate’ zircon (sample 73235,82; Pidgeon et al., 2007) in cross-polarised  
865 light and (b) in reflected light, the square indicates the location of the detailed images  
866 of the grains in Figure 8; (c) BSE image of zircon #5 from sample 73235,60 (a.k.a.  
867 ‘cracker’ grain). The dashed lines underline the limit of the anorthite clast. zrc =  
868 zircon; fsp = feldspar.

869

### 870 **Figure 2 – Zircon grown in the melt**

871 **Poikilitic zircon:** (a) BSE image of a zircon grain within meteorite sample SaU 169  
872 (courtesy of E. Gnos). **Acicular shape:** (b) BSE image of zircon #2 from sample  
873 73217,52 (Grange et al., 2009), the zircon is outlined by a dashed line, the other bright  
874 needle-like minerals are ilmenite; K-feldspar, shown with an arrow, are the small  
875 acicular features within the glass. Same abbreviations as in Figure 1. plg =  
876 plagioclase; px = pyroxene; ilm = ilmenite.

877

878

### 879 **Figure 3 – Zircon clasts in breccia matrix**

880 (a) BSE image of the zircon #3 from sample 73235,59 (a.k.a. ‘tiger’ zircon); the black  
881 arrows indicate recrystallised zones (see text for details); (b) CL image of the zircon  
882 from sample 76295,91 (a.k.a. ‘arrowhead’ zircon); the bright lines are gold coating  
883 filling the fractures of the grain; (c) BSE image of the zircon #3 from sample  
884 73235,60; (d) BSE image of the zircon #1 from sample 14305,93.

885

### 886 **Figure 4 – Internal structures of magmatic grains**

887 **Oscillatory zoning:** Images of zircon #1 from sample 14083,35 (a.k.a. ‘teardrop’  
888 zircon) in (a) cross-polarised light and (b) CL, the insert shows details of the  
889 oscillatory zoning, the white arrow shows the sector zoning; images of zircon #1 from  
890 sample 14303,49 in (c) cross-polarised light and (d) CL; (e) CL image of a zircon  
891 grain extracted from A14 soil. **Sector zoning:** (f) detail of the zircon from 73235,82  
892 (a.k.a. ‘pomegranate’ zircon; Pidgeon et al., 2007) in CL; (g) CL image of the zircon  
893 #1 from 14306,60; (h) CL image of the zircon #2 from 14306,60. **No zoning**  
894 **(homogenous grain):** (i) BSE image of the zircon #4 from sample 73235,60 (a.k.a.

895 ‘hexagon’ zircon); **(j)** cumulative misorientation map obtained by EBSD on the  
896 73235,60#4. Same abbreviations as in Figure 1 and qtz = quartz; K-fs = K-feldspar;  
897 cpx = clinopyroxene; opx = orthopyroxene.

898

#### 899 **Figure 5 – Ages of magmatic grains**

900 Age of a zircon with oscillatory and sector zoning: the ‘teardrop’ (sample  
901 14083,35#1; [Table 2](#)), **(a)** weighted average; **(b)** normal concordia diagram. Age of an  
902 homogenous grain: the ‘hexagon’ (sample 73235,60#4; Grange et al., 2011), **(c)**  
903 weighted average; **(d)** normal concordia diagram. Errors are given at the 95% conf.  
904 level; boxes and ellipses are drawn at  $2\sigma$  with Isoplot (Ludwig, 2008).

905

#### 906 **Figure 6 – Zircon with recrystallised zones**

907 **(a)** CL image of the ‘tiger’ grain (sample 73235,59#3) showing two brightly  
908 luminescent recrystallised zones of secondary zircon; **(b)** BSE image of the zircon-  
909 baddeleyite aggregate from sample 73217,52 (zircon type-3, Grange et al., 2009), the  
910 zircon formed from a reaction between baddeleyite and surrounding Si-rich melt.

911

#### 912 **Figure 7 – Ages of zircons with primary and secondary parts**

913 **(a)** Concordia diagram of the ‘tiger’ grain; **(b)** Concordia diagram of the pomegranate  
914 grain with matrix vs fragments (after Pidgeon et al., 2007). The ages reported for the  
915 primary magmatic (Zrc I) and secondary impact (Zrc II) zircon are weighted average  
916  $^{207}\text{Pb}/^{206}\text{Pb}$  ages with errors at the 95% conf. level; the white ellipses are those not  
917 used in the age calculation; ellipses have been drawn at  $2\sigma$  with Isoplot (Ludwig,  
918 2008). Data after Grange et al. (2011).

919

#### 920 **Figure 8 – Loss of crystallinity**

921 Primary fragments **(a)** CL image of a part of the ‘pomegranate’ zircon (as shown in  
922 Figure 1b) showing sector zoning (see scale and legend in (c)), the dashed line  
923 indicates the limit between the zircon and the surrounding plagioclase (plg) of the  
924 anorthite clast, zrc I correspond to primary zircon “fragments” (see text) and zrc II  
925 corresponds to secondary zircon “matrix”; **(b)** SE image of a piece of the  
926 ‘pomegranate’ zircon, illustrating the difference in relief between zircon I and II,  
927 plagioclase appears in black, the square corresponds to the field of view of (e); **(c)**  
928 EBSD map of the same part of the ‘pomegranate’ grain as shown in (a) and (c), the

929 similar colour correspond to similar crystalline orientation (the Euler colors are  
930 defines by 3 colors channels assigned to 3 Euler angles to describe orientation; Prior  
931 et al., 1999); **(d)** cumulative misorientation (in degrees from the red cross) derived  
932 from EBSD measurements of the ‘propeller’ grain, the arrows show parts of the  
933 secondary zircon (zrc II) that are not indexed in EBSD and appear in black, the  
934 dashed line delimits the zircon; **(e)** SE image of the ‘propeller’ grain, the top of the  
935 image corresponding to the edge of the thin section has been hidden with a black  
936 cover to reduce the brightness resulting of the high relief of the edge, the arrows point  
937 toward the most obvious differences in relief between zrc I and II.

938

939 **Figure 9 – U and Th content vs ages for both pomegranate and ‘propeller’ grains**  
940 **(a)** Th/U vs ages for the two parts of the ‘pomegranate’ zircon; **(b)** Th/U vs U content  
941 of the ‘pomegranate’ grain, the ellipse includes the data with U<40 ppm (see text); **(c)**  
942 Th/U vs ages for the ‘propeller’ grain, the two zrc II analyses have been obtained on  
943 the least crystalline parts of the grain; **(d)** Th/U vs U content of the ‘propeller’ zircon.  
944 (data after [Table 2](#) and Pidgeon et al., 2007; Grange et al., 2011).

945

946 **Figure 10 – Ductile (crystal-plastic) deformation**

947 Cumulative misorientation derived from EBSD mapping for **(a)** the ‘tiger’ zircon  
948 (sample 73235,59); **(b)** the ‘oldest’ zircon (sample 72215,195, Nemchin et al., 2009);  
949 **(c)** the ‘arrowhead’ zircon (sample 76295,195); the insert shows a set of planar  
950 features (underlined by the dashed line) that is not seen under an optical microscope  
951 (see text for details). For every image, the colours reflect the cumulative  
952 crystallographic misorientation in degrees from a reference orientation indicated by  
953 the cross.

954

955 **Figure 11 – Concordia of the ‘propeller’ zircon**

956 The white ellipses represent analyses obtained on the primary zircon (zrc I) while the  
957 analyses made on the secondary zircon (zrc II) are shown in grey ellipses. The  
958 weighted average of the two analyses of zrc II is  $4308 \pm 11$  Ma (95 % conf. level) and  
959 probably represents a maximum age for the impact event. The ages of zrc I overlap  
960 this mean and range from 4305 to 4378 Ma ([Table 2](#)).

961

962 **Figure 12 – Planar features**

963 Planar features as seen with optical microscope in cross-polarised light: (a) image of  
964 the ‘tiger’ zircon (sample 73235,59); (b) image of the ‘arrowhead’ zircon (sample  
965 76295,91); (c) image of zircon #62 from sample 14306,60 (U-Pb not analysed).  
966 (d) Planar features of the ‘tiger’ zircon (73235,59) evidenced by EBSD pattern quality  
967 (band contrast) map. Grain is shaded from poor (black) to good (white) EBSD pattern  
968 quality. (e) Planar features of zircon #3 from sample 14303,49 imaged by CL.

969

### 970 **Figure 13 – Fractures**

971 Cumulative misorientation map derived from EBSD mapping of the ‘cracker’ zircon  
972 (zircon #5 from sample 73235,60); the black lines delimit the domains of similar  
973 lattice orientation and correspond to the fractures affecting the grain as seen in Figure  
974 1c. The grain is coloured for cumulative crystallographic misorientation in degrees  
975 from a reference orientation indicated by the cross.

976

### 977 **Figure 14 – Concordia of fractured zircons**

978 (a) Concordia diagram of the ‘cracker’ zircon (sample 73235,60 zircon #5) showing  
979 the scatter of ages along the concordia curve (Grange et al., 2011); (b) Concordia  
980 diagram of the zircon #1 from sample 14303,49; analyses #5 and #9 are the most  
981 discordant, while analyse #3 is both concordant and the oldest and therefore probably  
982 represents the best estimate of the zircon crystallisation age (Table 2); (c) BSE image  
983 of the zircon #1 from sample 14303,49 showing the location of the three spots  
984 evidenced in the concordia diagram shown in (b); the inserts are SE images of the 3  
985 spots, with spots #5 and #9 clearly located across small fractures whereas spot #3 is  
986 located in a non-fractured zone of the zircon.

987

### 988 **Figure 15 – Zircon U-Pb phenomena cartoon**

989 Schematic representation of the behaviour of U-Pb systems in lunar zircon in relation  
990 with observed microstructure. The small ellipses drawn on the grains represent the ion  
991 microprobe analyses and refer to the age ellipses reported on the concordia diagrams  
992 below. See text for details.



**Table 1: description of new zircon grains**

Sample Name	Size ( $\mu\text{m}$ )	Habit	TEXTURE	STRUCTURE					
				Internal Zoning <i>as seen in CL</i>	Recrystallisation	Loss of Crystallinity	Ductile deformation <i>in degrees of misorientation</i>	Discrete planar features	Fractures
<b>APOLLO 17</b>									
73215,122 #6 (propeller)	200x25	anhedral with 3 "arms"	enclosed in plagioclase grains	no	no	at the tips of the arms	22°	no	no
76295,91 #2 (arrowhead)	300x100	anhedral	matrix	sector zoning	no	no	15°	5 sets	no
<b>APOLLO 14</b>									
14083,35 #1 (teardrop)	350x200	subhedral	matrix	sector and oscillatory zoning	no	no	N/A	no	no
14163 #10 (soil sample)	100x50	subhedral (broken)	in the soil	oscillatory zoning	no	no	N/A	no	no
14303,49 #1	1200x350	anhedral	granite clast	oscillatory zoning	no	no	N/A	no	yes
14303,49 #3 (*)	70x70	anhedral	matrix	no	no	no	N/A	1 set	no
14305,93 #1	80x70	anhedral	matrix	sector zoning	no	no	N/A	no	no
14306,60 #1 (simcard)	200x160	subhedral	clast	sector and oscillatory zoning	no	no	N/A	no	no
14306,60 #2	330x150	subhedral	matrix	sector zoning	no	no	N/A	no	no
14306,60 #62 (*)	120x80	anhedral	matrix	no	no	no	N/A	2 sets	no
14321,1613 #1	170x130	anhedral	N/A	faint sector zoning	no	partly metamict	N/A	no	no
14321,1613 #2	100x70	anhedral	N/A	faint sector zoning	no	partly metamict	N/A	no	no

(\*) no U-Pb data for this grain

Table 2: U-Pb results for zircon

Samples	U (ppm)	Th (ppm)	Th/U	Pb* (ppm)	$\frac{^{206}\text{Pb}}{^{204}\text{Pb}}$	$\frac{^{207}\text{Pb}}{^{206}\text{Pb}}$	err % 1 $\sigma$	$\frac{^{238}\text{U}}{^{206}\text{Pb}}$	err % 1 $\sigma$	$\frac{^{207}\text{Pb}^*}{^{235}\text{U}}$	err % 1 $\sigma$	$\frac{^{206}\text{Pb}^*}{^{238}\text{U}}$	err % 1 $\sigma$	$\rho$ (c)	$\frac{^{207}\text{Pb}^*}{^{206}\text{Pb}^*}$	err % 1 $\sigma$	$\frac{^{207}\text{Pb}^*}{^{206}\text{Pb}^*}$
					(b)	total		total		total		total			(age Ma)		
<b>Zircon-spots</b>																	
<b>APOLLO 17</b>																	
<b>73215,122</b>																	
<b>zircon #6 - propeller</b>																	
122-6-1	94	29	0.31	75	29020	0.5178	1.41	1.078	1.75	66.15	2.25	0.927	1.75	0.78	0.5176	1.41	4292 $\pm$ 21
122-6-2	64	28	0.43	51	1940	0.5288	0.48	1.074	1.79	66.84	1.87	0.922	1.80	0.96	0.5256	0.50	4315 $\pm$ 7
122-6-3	58	26	0.44	48	5920	0.5371	0.47	1.043	1.82	70.66	1.89	0.956	1.82	0.97	0.5360	0.47	4344 $\pm$ 7
122-6-4	46	18	0.39	37	1940	0.5325	1.24	1.060	1.86	68.24	2.25	0.935	1.87	0.83	0.5293	1.26	4325 $\pm$ 18
122-6-5	52	21	0.41	43	9120	0.5483	1.21	1.025	1.86	73.53	2.22	0.974	1.86	0.84	0.5476	1.21	4375 $\pm$ 18
122-6-6	46	18	0.39	38	3840	0.5430	2.93	1.050	1.87	70.75	3.50	0.948	1.87	0.54	0.5415	2.96	4358 $\pm$ 43
122-6-7	59	23	0.39	49	7430	0.5495	1.41	1.031	1.83	73.19	2.32	0.967	1.83	0.79	0.5488	1.42	4378 $\pm$ 21
122-6-8	72	26	0.37	60	18930	0.5225	0.45	1.021	1.83	70.47	1.89	0.979	1.83	0.97	0.5222	0.45	4305 $\pm$ 7
122-6-9	58	22	0.39	47	5750	0.5319	0.46	1.053	1.83	69.31	1.89	0.947	1.83	0.97	0.5308	0.47	4329 $\pm$ 7
122-6-10	100	34	0.34	81	5880	0.5247	0.41	1.064	2.07	67.63	2.11	0.937	2.07	0.98	0.5236	0.42	4309 $\pm$ 6
122-6-11 (1-1) (a)	65	27	0.42	107	9520	0.5387	0.48	0.995	1.11	74.39	1.30	1.003	1.20	0.93	0.5381	0.48	4349 $\pm$ 7
122-6-12 (1-2) (a)	68	28	0.42	110	34320	0.5292	0.34	1.012	1.19	72.04	1.30	0.988	1.20	0.97	0.5290	0.34	4324 $\pm$ 5
122-6-13 (1-3) (a)	71	27	0.38	117	6170	0.5315	0.57	0.986	1.12	73.98	1.30	1.011	1.20	0.91	0.5305	0.57	4328 $\pm$ 8
<b>76295,91</b>																	
<b>zircon #2 - arrowhead (**)</b>																	
91-1	59	39	0.67	48	13353	0.4715	0.28	1.073	1.70	60.46	1.73	0.931	1.70	0.99	0.4709	0.29	4153 $\pm$ 4
91-2	61	38	0.64	48	12092	0.4699	0.28	1.105	1.70	58.49	1.72	0.904	1.70	0.99	0.4693	0.28	4148 $\pm$ 4
91-3	55	31	0.57	43	17350	0.4702	0.53	1.094	1.70	59.15	1.78	0.913	1.70	0.95	0.4698	0.53	4149 $\pm$ 8
91-4	53	36	0.71	42	109431	0.4710	0.28	1.069	1.71	60.73	1.73	0.935	1.71	0.99	0.4709	0.29	4153 $\pm$ 4
91-5	55	32	0.60	43	201943	0.4762	0.29	1.101	1.71	59.63	1.73	0.908	1.71	0.99	0.4762	0.29	4169 $\pm$ 4
91-6	43	25	0.60	32	11946	0.4732	0.35	1.144	1.72	56.88	1.76	0.873	1.73	0.98	0.4726	0.35	4158 $\pm$ 5
91-7	40	23	0.61	31	29570	0.4614	0.59	1.108	1.73	57.35	1.83	0.902	1.73	0.95	0.4612	0.59	4122 $\pm$ 9
91-8	73	43	0.60	51	-	0.4900	0.37	1.219	1.71	55.48	1.75	0.821	1.71	0.98	0.4902	0.37	4212 $\pm$ 5
91-9	72	46	0.67	54	16561	0.4859	0.34	1.141	1.73	58.60	1.77	0.875	1.73	0.98	0.4855	0.34	4198 $\pm$ 5
91-10	58	33	0.59	41	13184	0.4770	0.41	1.209	1.73	54.28	1.79	0.826	1.74	0.97	0.4765	0.43	4170 $\pm$ 6
91-11 (m91.1)	55	33	0.63	42	16401	0.4579	0.59	1.122	2.43	56.14	2.50	0.890	2.43	0.97	0.4575	0.60	4110 $\pm$ 9
91-12 (m91.2)	54	30	0.58	44	6527	0.5129	0.58	1.043	2.45	67.50	2.52	0.956	2.45	0.97	0.5120	0.58	4276 $\pm$ 9
91-13 (m91.3)	40	23	0.59	31	-	0.5002	0.81	1.100	2.54	62.91	2.67	0.911	2.54	0.95	0.5008	0.81	4243 $\pm$ 12
91-14 (m91.4)	52	34	0.68	40	10381	0.4695	0.68	1.130	2.42	57.10	2.52	0.883	2.43	0.96	0.4688	0.68	4146 $\pm$ 10
91-15 (m91.5)	60	39	0.66	47	17261	0.4975	0.62	1.091	2.40	62.76	2.48	0.916	2.40	0.97	0.4971	0.62	4233 $\pm$ 9
91-16 (m91.6)	40	23	0.59	31	15763	0.4945	1.26	1.094	2.59	62.17	2.88	0.913	2.59	0.90	0.4941	1.27	4224 $\pm$ 19
91-17 (m91.7)	55	35	0.65	41	8768	0.4956	1.73	1.152	2.39	59.11	2.95	0.866	2.39	0.81	0.4948	1.74	4226 $\pm$ 26
<b>APOLLO 14</b>																	
<b>14083,35</b>																	
<b>zircon #1 - teardrop</b>																	
083-35-101	113	84	0.77	82	161112	0.4358	0.20	1.193	0.69	50.36	0.72	0.838	0.69	0.96	0.4357	0.21	4037 $\pm$ 3
083-35-102	63	46	0.76	46	36613	0.4371	0.45	1.163	0.76	51.78	0.91	0.860	0.78	0.86	0.4368	0.47	4041 $\pm$ 7
083-35-103	80	69	0.89	58	14408	0.4381	0.25	1.184	0.75	50.91	0.79	0.844	0.75	0.95	0.4375	0.25	4043 $\pm$ 4

**Table 2: U-Pb results for zircon**

Samples	U (ppm)	Th (ppm)	Th/U	Pb* (ppm)	$\frac{^{206}\text{Pb}}{^{204}\text{Pb}}$	$\frac{^{207}\text{Pb}}{^{206}\text{Pb}}$	err % 1 $\sigma$	$\frac{^{238}\text{U}}{^{206}\text{Pb}}$	err % 1 $\sigma$	$\frac{^{207}\text{Pb}^*}{^{235}\text{U}}$	err % 1 $\sigma$	$\frac{^{206}\text{Pb}^*}{^{238}\text{U}}$	err % 1 $\sigma$	$\rho$ (c)	$\frac{^{207}\text{Pb}^*}{^{206}\text{Pb}^*}$	err % 1 $\sigma$	$\frac{^{207}\text{Pb}^*}{^{206}\text{Pb}^*}$	
					(b)	total		total		total		(age Ma)						
<b>Zircon-spots</b>																		
083-35-104	52	35	0.70	39	18859	0.4358	0.31	1.154	1.14	51.97	1.18	0.866	1.14	0.97	0.4354	0.31	4036 $\pm$ 5	
083-35-105	48	37	0.80	36	-	0.4363	0.31	1.140	0.87	52.83	0.93	0.878	0.88	0.94	0.4365	0.32	4040 $\pm$ 5	
083-35-106	73	68	0.97	53	28230	0.4371	0.27	1.174	1.52	51.27	1.55	0.851	1.52	0.98	0.4368	0.28	4041 $\pm$ 4	
<b>14163 (soil)</b>																		
163-10	103	73	0.61	162	34070	0.5357	0.47	1.083	1.20	68.19	1.29	0.923	1.20	0.93	0.5357	0.47	4343 $\pm$ 7	
<b>14303,49 zircon #1</b>																		
303-49-101	88	31	0.37	72	6889	0.5157	0.24	1.047	0.96	67.61	0.99	0.953	0.96	0.97	0.5148	0.25	4284 $\pm$ 4	
303-49-102	112	48	0.44	89	946	0.5286	0.20	1.060	0.91	66.65	0.94	0.926	0.92	0.97	0.5220	0.22	4304 $\pm$ 3	
303-49-103	128	58	0.47	104	25198	0.5346	0.19	1.053	0.91	69.92	0.93	0.949	0.91	0.98	0.5343	0.19	4339 $\pm$ 3	
303-49-104	70	25	0.37	57	1710	0.5303	0.25	1.049	0.98	68.53	1.03	0.944	0.99	0.97	0.5267	0.27	4318 $\pm$ 4	
303-49-105	70	25	0.37	53	851	0.5033	0.38	1.112	0.98	60.16	1.08	0.881	1.00	0.92	0.4954	0.41	4228 $\pm$ 6	
303-49-106	61	21	0.35	51	3126	0.5312	0.27	1.018	1.00	71.25	1.04	0.976	1.01	0.96	0.5292	0.28	4325 $\pm$ 4	
303-49-107	81	30	0.39	66	6734	0.5289	0.23	1.051	0.96	69.10	0.99	0.949	0.96	0.97	0.5279	0.24	4321 $\pm$ 4	
303-49-108	65	24	0.38	53	8079	0.5298	0.27	1.062	0.99	68.52	1.03	0.939	0.99	0.97	0.5291	0.27	4324 $\pm$ 4	
303-49-109	82	33	0.42	63	42628	0.5063	0.24	1.111	1.01	62.80	1.05	0.900	1.02	0.97	0.5062	0.26	4259 $\pm$ 4	
<b>14305,93 zircon #1</b>																		
305-93-101	77	23	0.31	60	21498	0.4862	1.44	1.103	0.80	60.67	1.65	0.906	0.80	0.48	0.4858	1.44	4199 $\pm$ 21	
305-93-102	68	27	0.41	52	4504	0.4747	0.97	1.120	1.14	58.02	1.51	0.889	1.14	0.76	0.4731	0.98	4159 $\pm$ 15	
305-93-103	166	52	0.32	129	387621	0.4916	1.23	1.105	0.68	61.34	1.41	0.905	0.68	0.48	0.4916	1.23	4216 $\pm$ 18	
<b>14306,60 zircon #1 - simcard</b>																		
306-60-101	51	33	0.67	40	10187	0.4939	0.31	1.099	0.91	61.76	0.97	0.908	0.91	0.94	0.4932	0.32	4221 $\pm$ 5	
306-60-102	30	16	0.57	23	-	0.4880	0.40	1.081	1.61	62.28	1.66	0.926	1.61	0.97	0.4881	0.40	4206 $\pm$ 6	
306-60-103	19	6	0.35	16	62337	0.4887	0.51	1.058	1.32	63.64	1.41	0.945	1.32	0.93	0.4886	0.51	4207 $\pm$ 8	
306-60-104	23	9	0.42	19	233	0.5221	0.82	0.972	1.18	64.55	1.65	0.950	1.29	0.78	0.4929	1.03	4220 $\pm$ 15	
306-60-105	20	7	0.34	17	-	0.4920	0.50	1.056	1.32	64.23	1.44	0.947	1.34	0.93	0.4920	0.54	4217 $\pm$ 8	
306-60-106	37	17	0.49	30	-	0.4855	0.38	1.042	1.01	64.27	1.10	0.960	1.02	0.93	0.4855	0.40	4198 $\pm$ 6	
<b>zircon #2</b>																		
306-60-201	13	4	0.35	10	4979	0.4893	1.16	1.096	2.59	61.18	2.86	0.909	2.60	0.91	0.4880	1.18	4205 $\pm$ 17	
306-60-202	13	4	0.35	10	814	0.4973	0.66	1.110	1.69	59.40	1.93	0.881	1.76	0.91	0.4889	0.79	4208 $\pm$ 12	
306-60-203	51	32	0.66	41	13581	0.4894	0.31	1.063	0.92	63.36	0.99	0.940	0.94	0.94	0.4889	0.34	4208 $\pm$ 5	
<b>14321,1613 zircon #1</b>																		
321-zrc1-1	352	192	0.55	473	32874	0.4171	0.26	1.160	1.38	49.59	1.40	0.862	1.38	0.98	0.4171	0.26	3972 $\pm$ 4	
321-zrc1-2	724	261	0.37	959	92183	0.4255	0.18	1.148	1.36	51.11	1.38	0.871	1.36	0.99	0.4255	0.18	4002 $\pm$ 3	
321-zrc1-3	569	196	0.35	751	323137	0.4227	0.23	1.145	1.39	50.89	1.41	0.873	1.39	0.99	0.4227	0.23	3992 $\pm$ 3	

**Table 2: U-Pb results for zircon**

Samples	U (ppm)	Th (ppm)	Th/U	Pb* (ppm)	$\frac{^{206}\text{Pb}}{^{204}\text{Pb}}$	$\frac{^{207}\text{Pb}}{^{206}\text{Pb}}$	err % 1 $\sigma$	$\frac{^{238}\text{U}}{^{206}\text{Pb}}$	err % 1 $\sigma$	$\frac{^{207}\text{Pb}^*}{^{235}\text{U}}$	err % 1 $\sigma$	$\frac{^{206}\text{Pb}^*}{^{238}\text{U}}$	err % 1 $\sigma$	$\rho$ (c)	$\frac{^{207}\text{Pb}^*}{^{206}\text{Pb}^*}$	err % 1 $\sigma$	$\frac{^{207}\text{Pb}^*}{^{206}\text{Pb}^*}$	
					(b)	total		total		total		(age Ma)						
Zircon-spots																		
321-zrc1-4	919	354	0.38	1202	101799	0.4226	0.23	1.161	1.36	50.17	1.38	0.861	1.36	0.99	0.4226	0.23	3992 $\pm$ 3	
321-zrc1-5	625	217	0.35	827	76289	0.4242	0.29	1.141	1.35	51.27	1.38	0.877	1.35	0.98	0.4242	0.29	3997 $\pm$ 4	
321-zrc1-6	518	167	0.33	703	43826	0.4261	0.29	1.111	1.37	52.91	1.40	0.900	1.37	0.98	0.4261	0.29	4004 $\pm$ 4	
<b>zircon #2</b>																		
321-zrc2-1	333	183	0.51	415	25252	0.4151	0.27	1.246	1.30	45.92	1.32	0.802	1.30	0.98	0.4151	0.27	3965 $\pm$ 4	
321-zrc2-2	326	178	0.51	407	63867	0.4135	0.34	1.241	1.30	45.93	1.34	0.806	1.30	0.97	0.4135	0.34	3959 $\pm$ 5	
321-zrc2-3	365	205	0.50	457	70770	0.4221	0.32	1.243	1.30	46.84	1.34	0.805	1.30	0.97	0.4221	0.32	3990 $\pm$ 5	
321-zrc2-4	986	542	0.48	1230	85604	0.4238	0.16	1.248	1.32	46.83	1.33	0.802	1.32	0.99	0.4238	0.16	3996 $\pm$ 2	

\* indicates radiogenic Pb, i.e. corrected from common Pb (after Stacey and Kramers, 1975)

\*\* Data on arrowhead zircon have been obtained in 2003 (spot name starting with m) and 2009

(a) data published in Nemchin et al. (2008) as the name shown in bracket

(b) (-) indicate that the amount of  $^{204}\text{Pb}$  is too small to give a significant ratio

(c) error correlation between ( $^{235}\text{U}/^{207}\text{Pb}^*$ ) and ( $^{238}\text{U}/^{206}\text{Pb}^*$ )

Errors on individual age are given at 1 $\sigma$

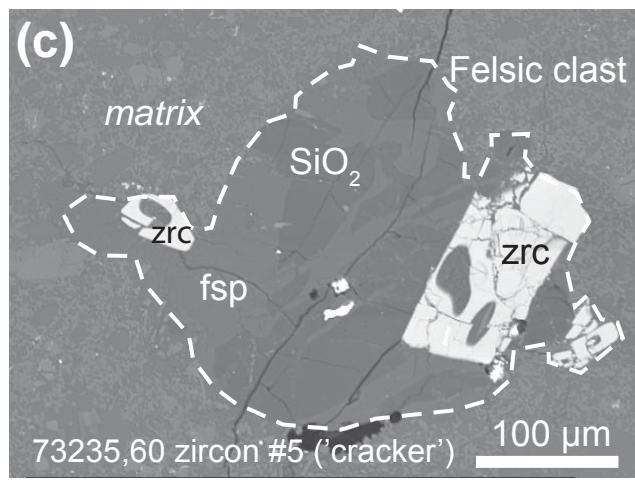
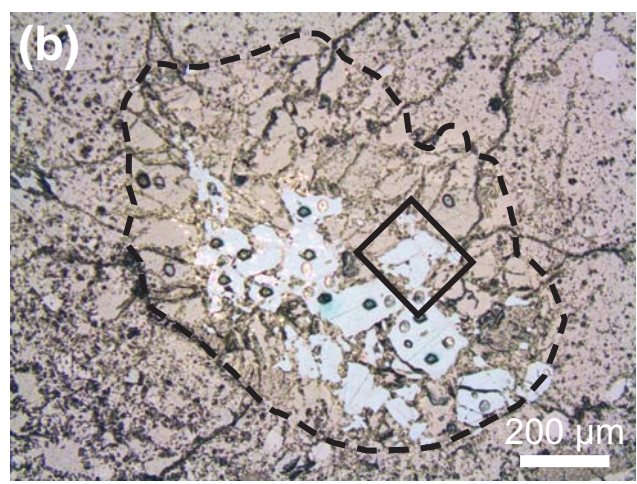
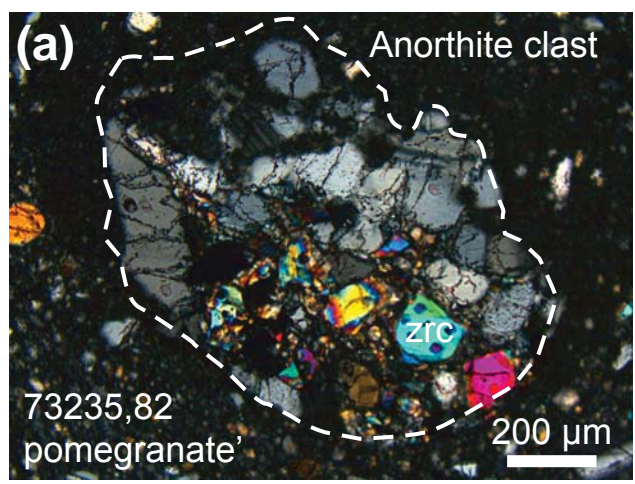


**Figure 1**

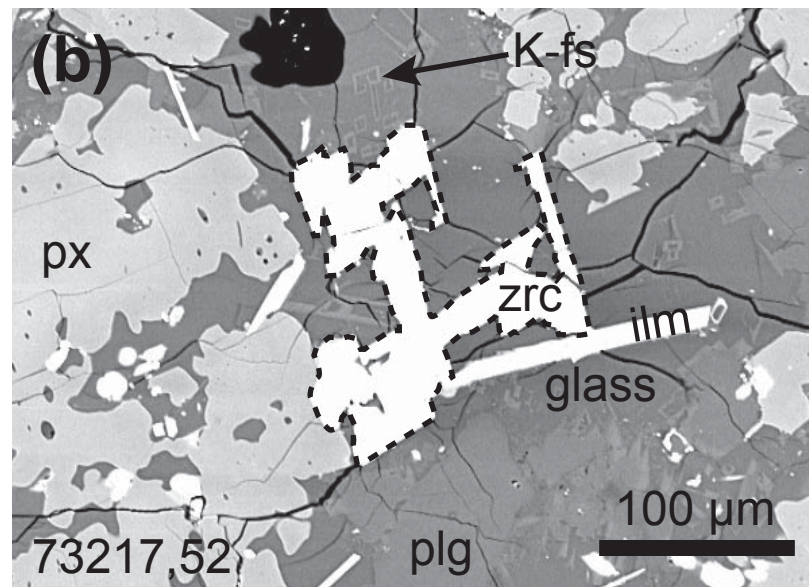
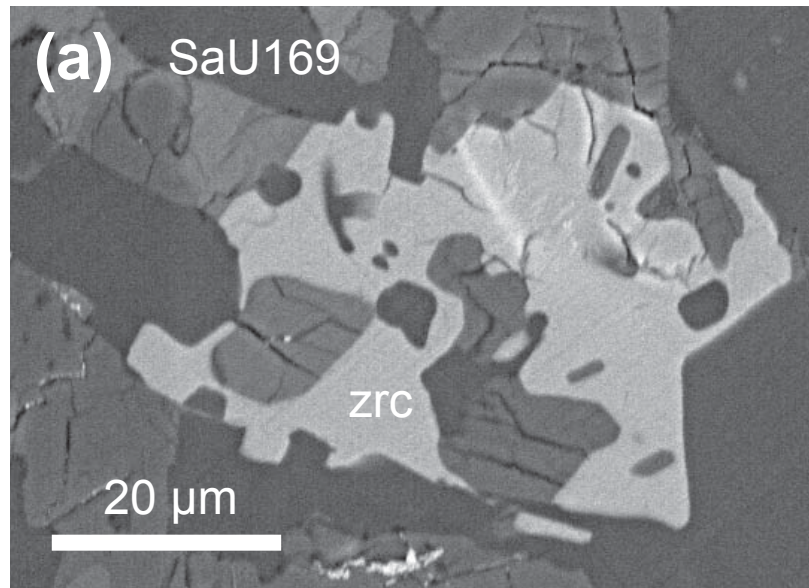
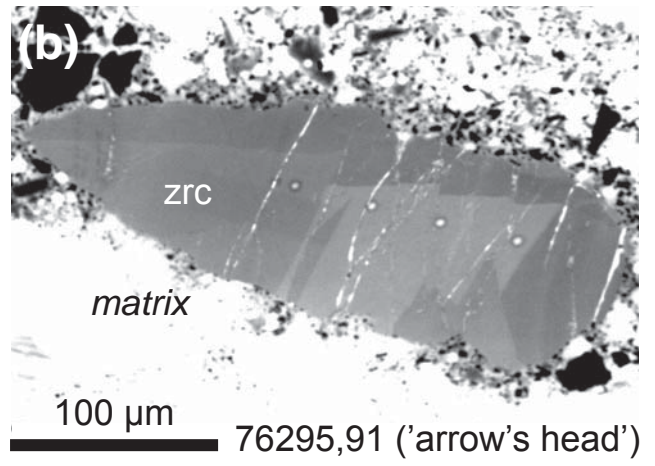
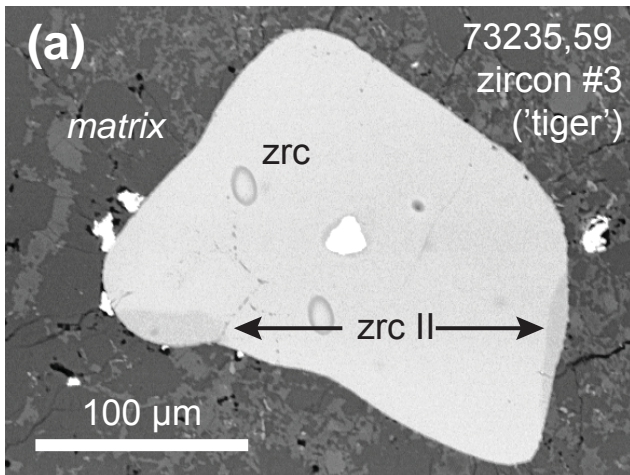


**Figure 2**



## Big grains



## Small grains

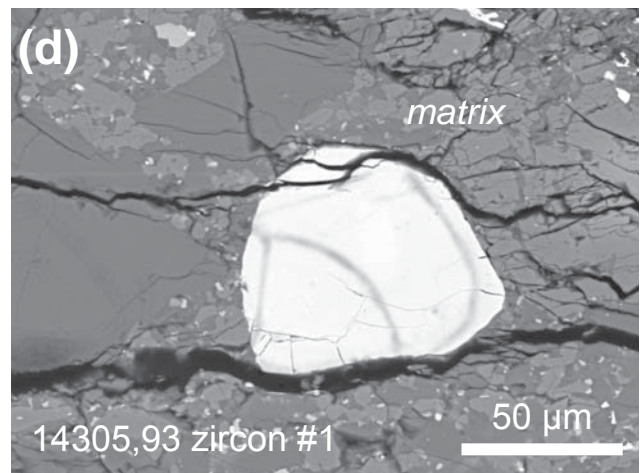
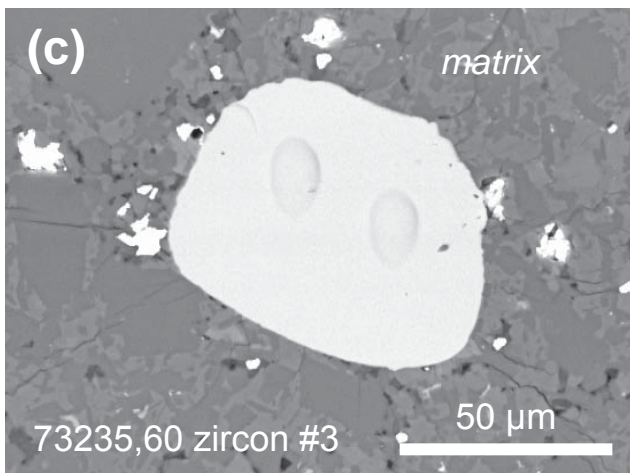
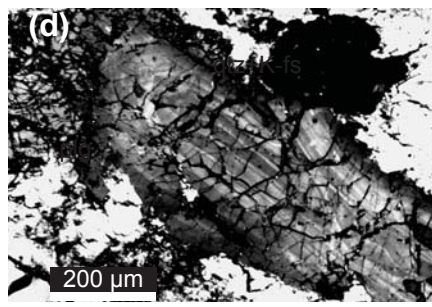
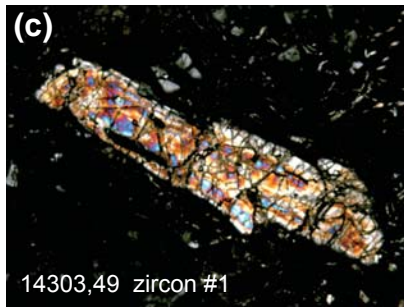
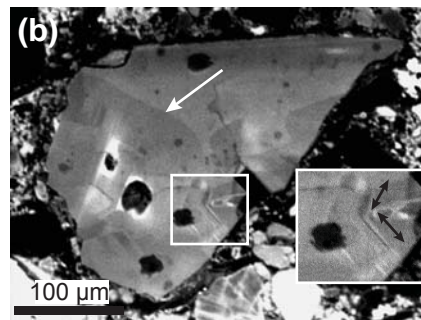
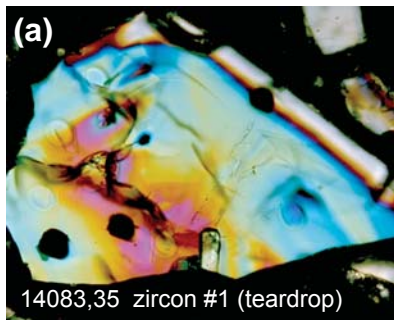
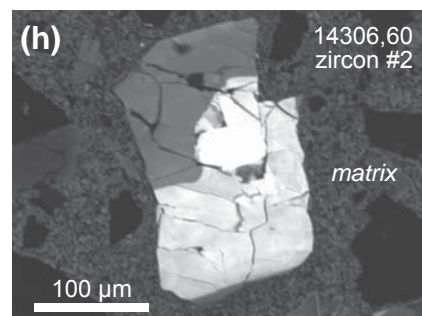
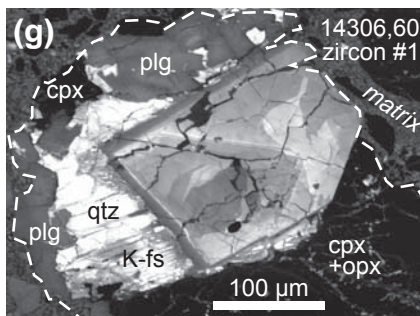
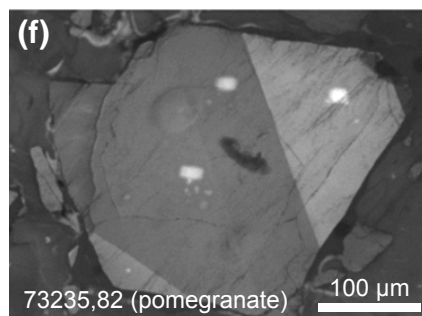


**Figure 3**

## Oscillatory Zoning



## Sector Zoning



## No zoning (homogenous grain)

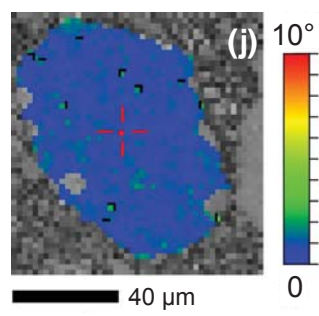
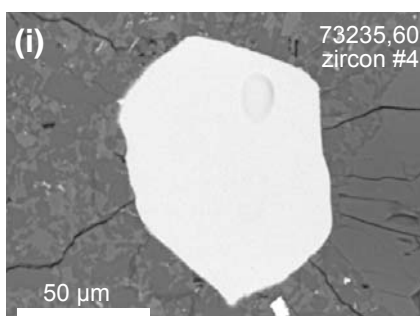
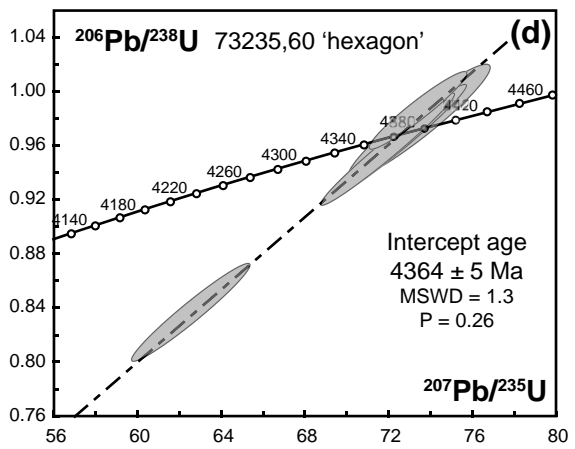
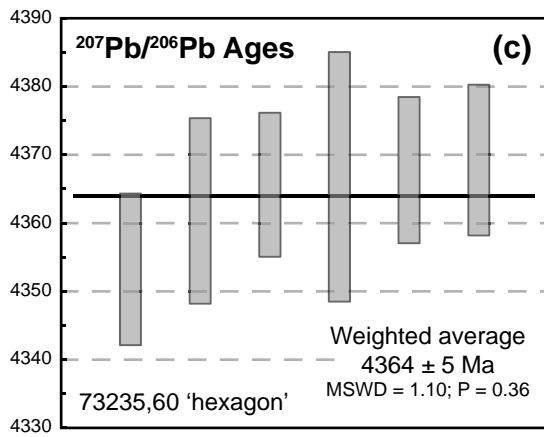
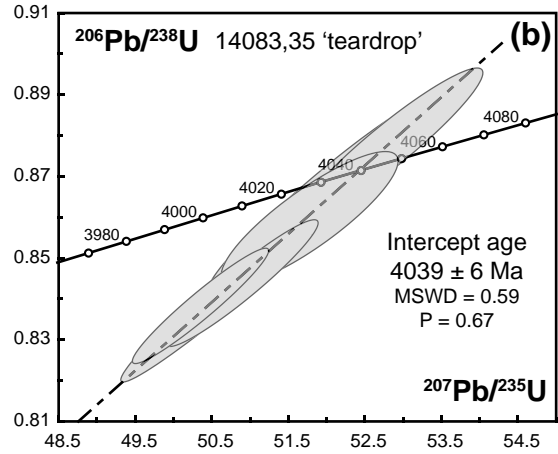
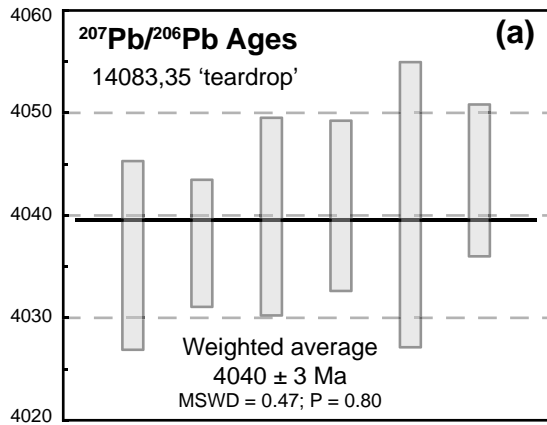
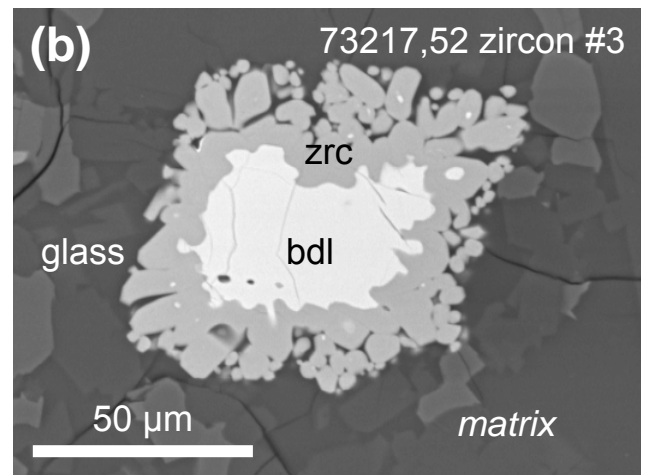
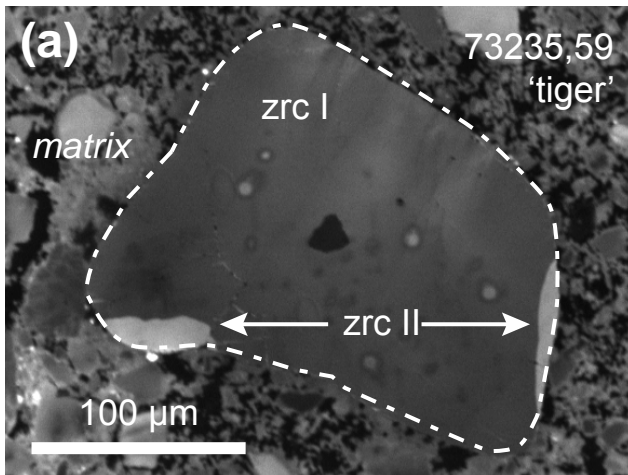


Figure 4





**Figure 05**



**Figure 6**

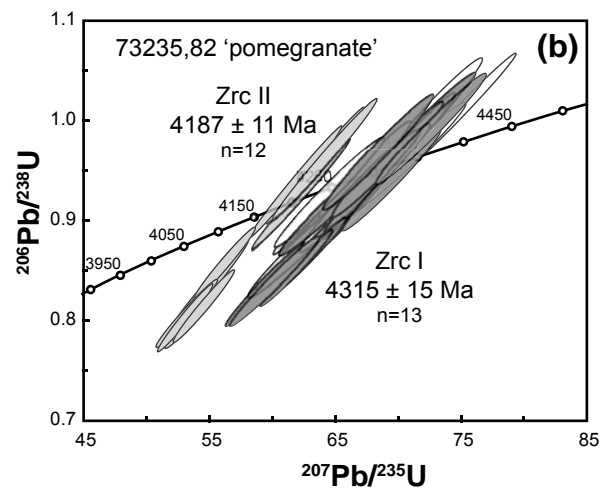
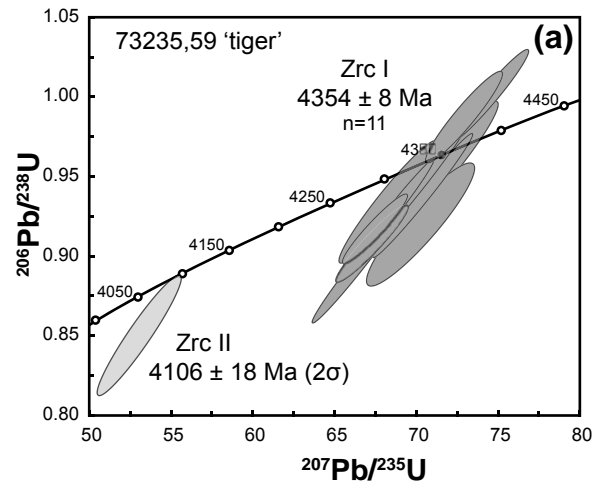
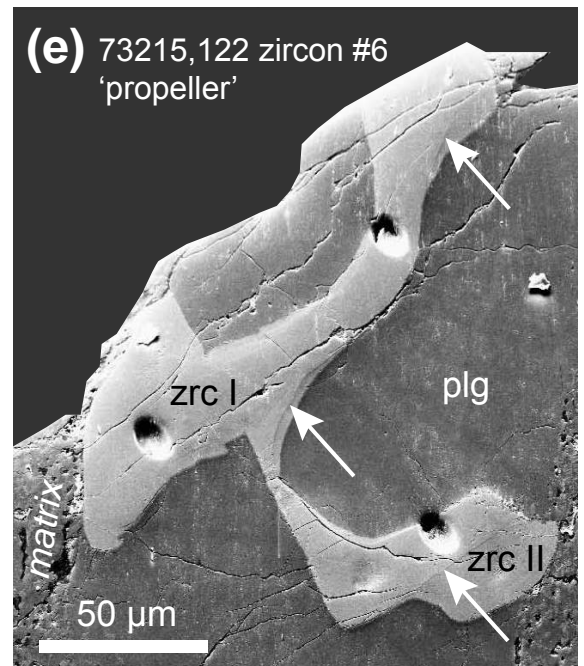
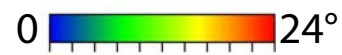
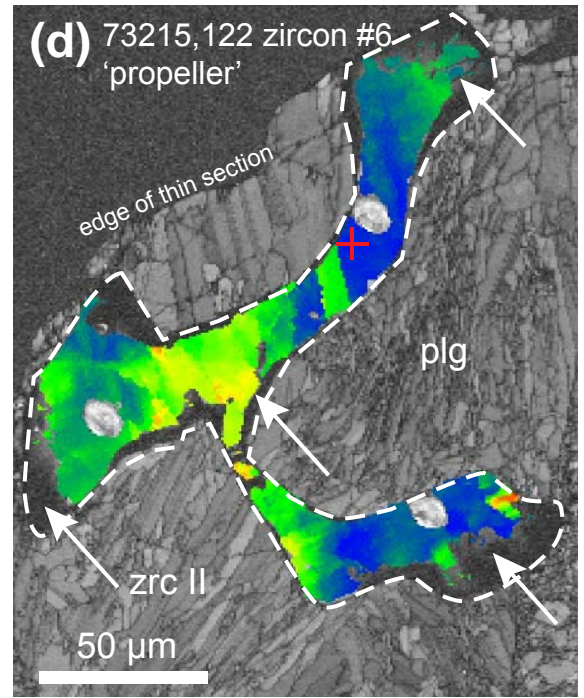
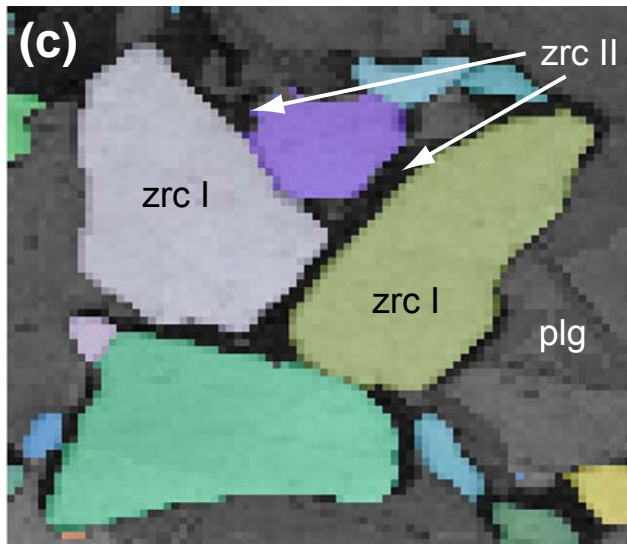
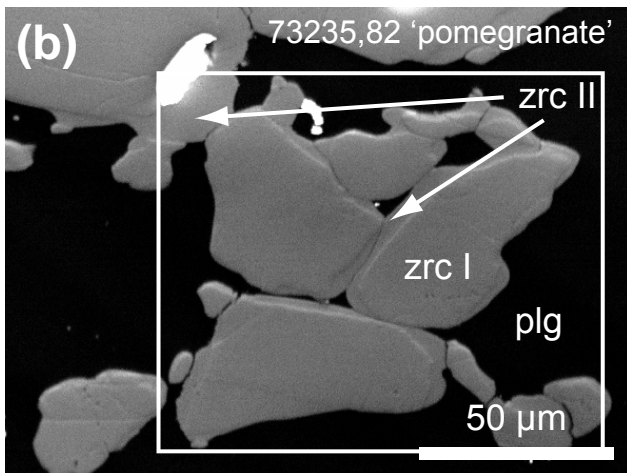
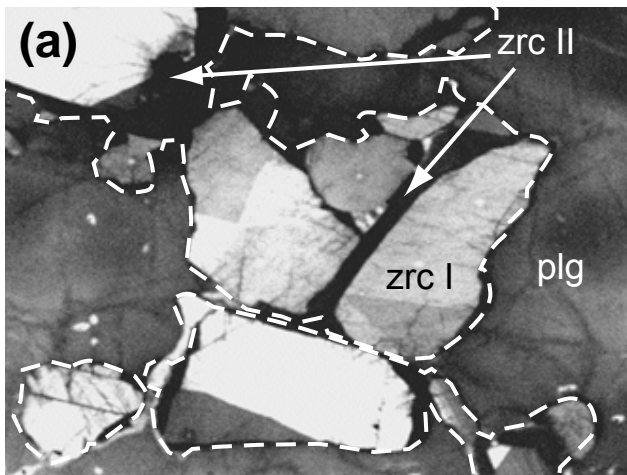
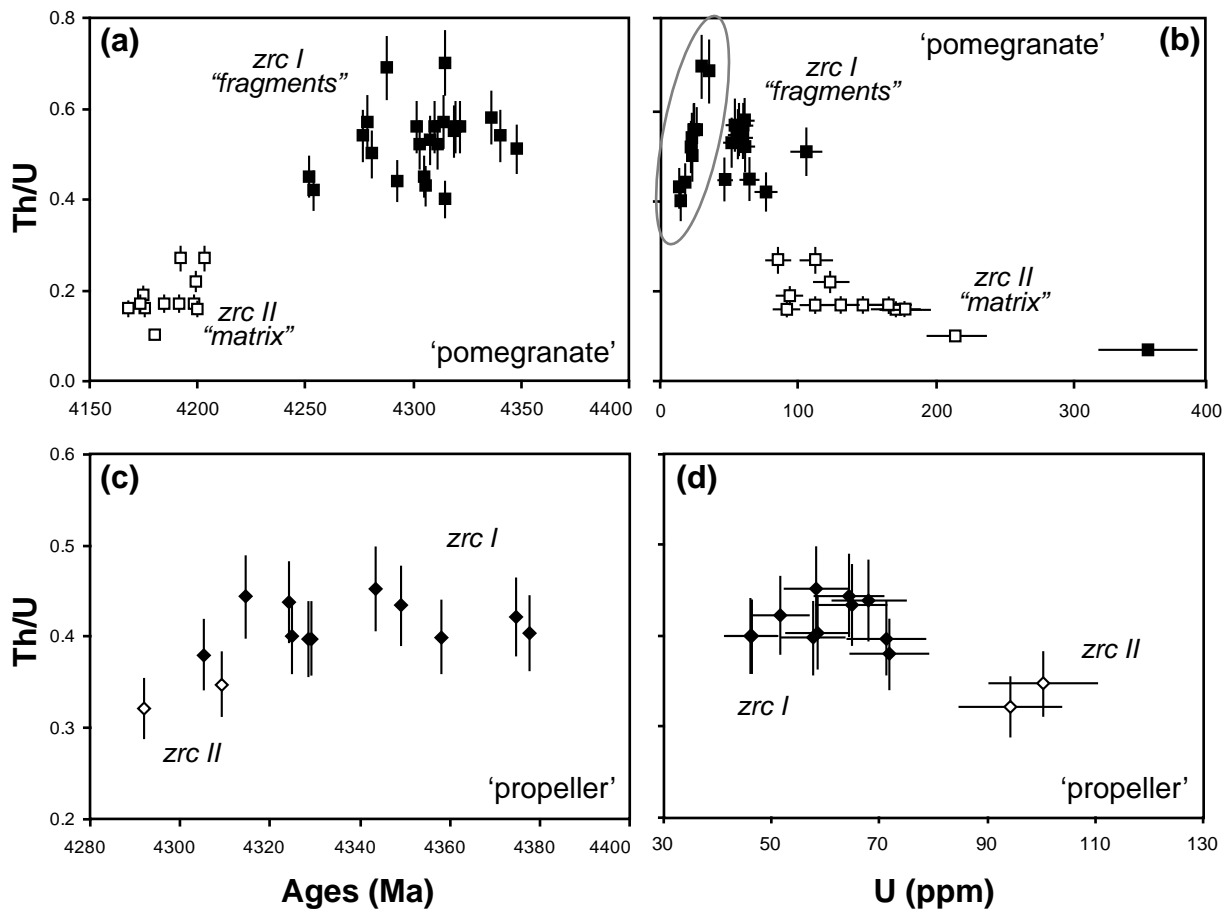


Figure 7



**Figure 8**



**Figure 9**



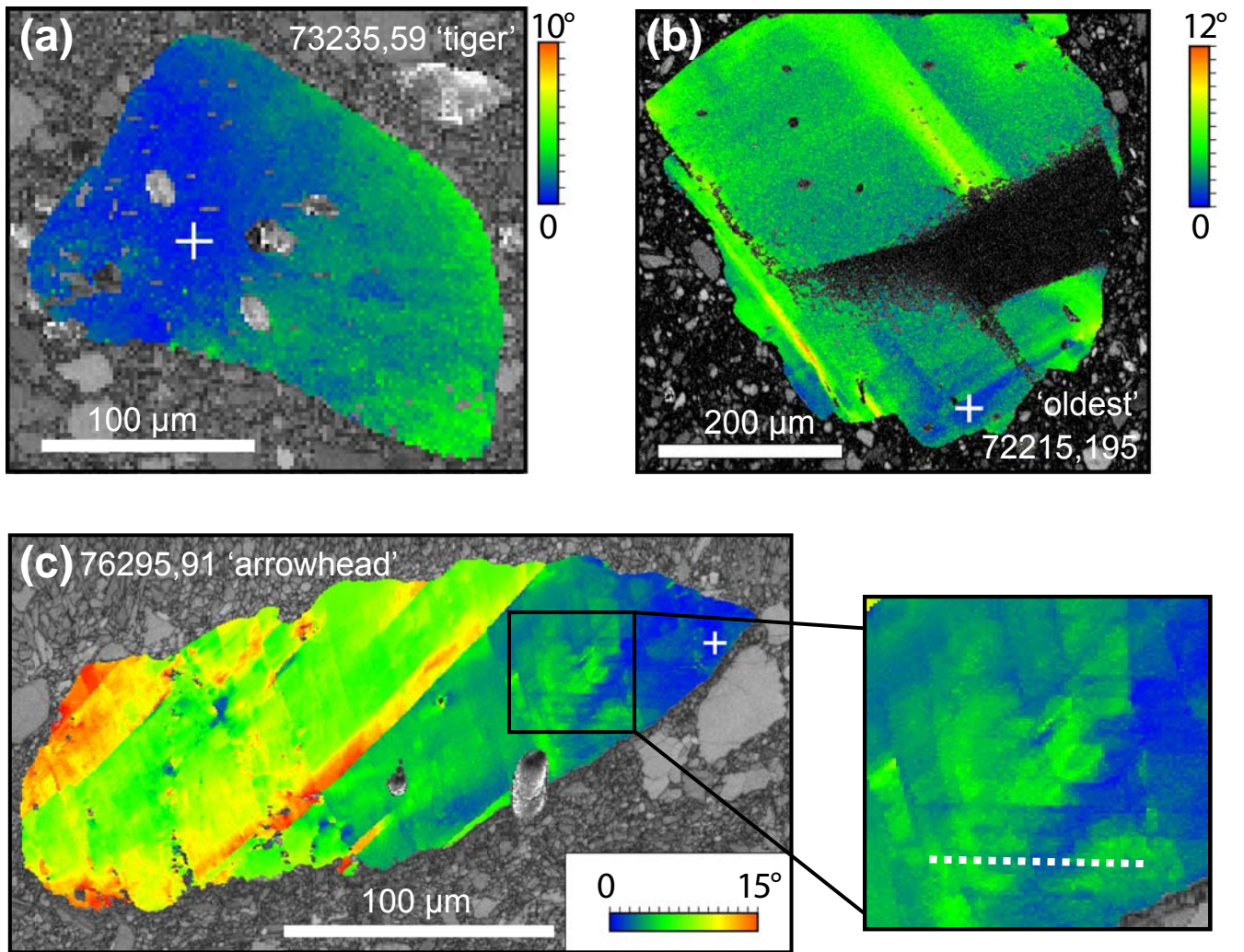


**Figure 10**

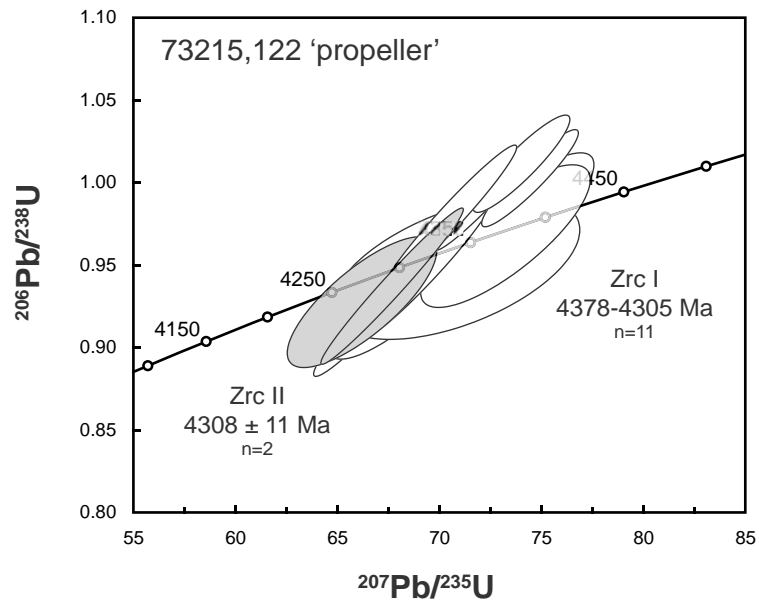


**Figure 11**

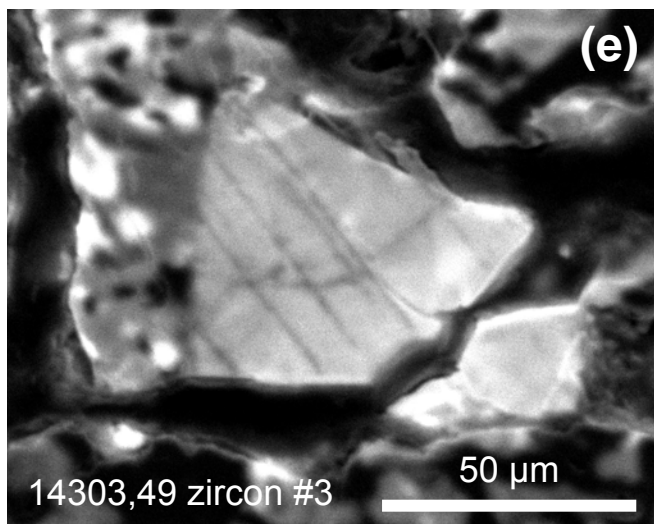
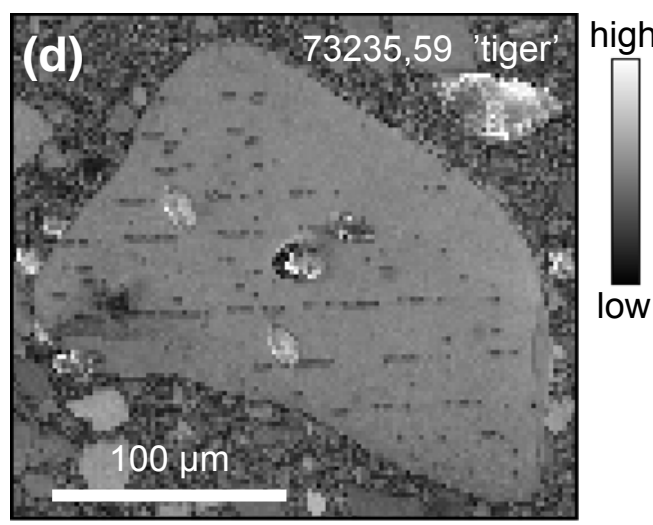
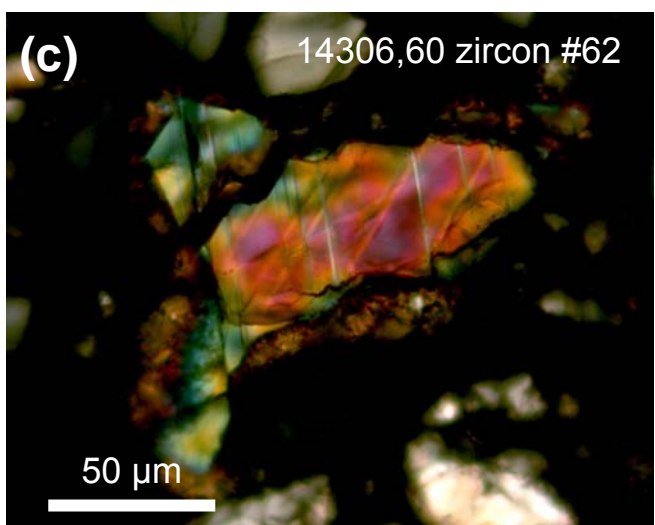
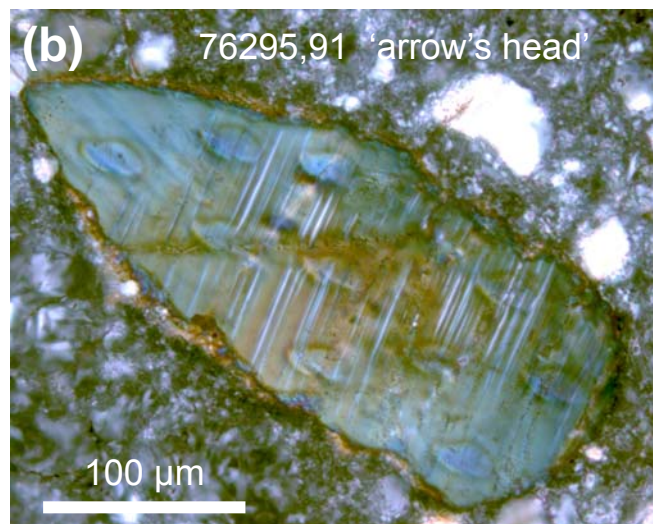
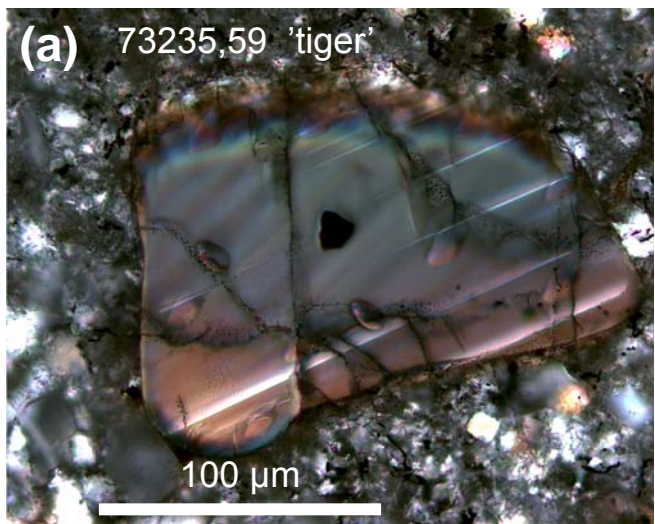


**Figure 12**



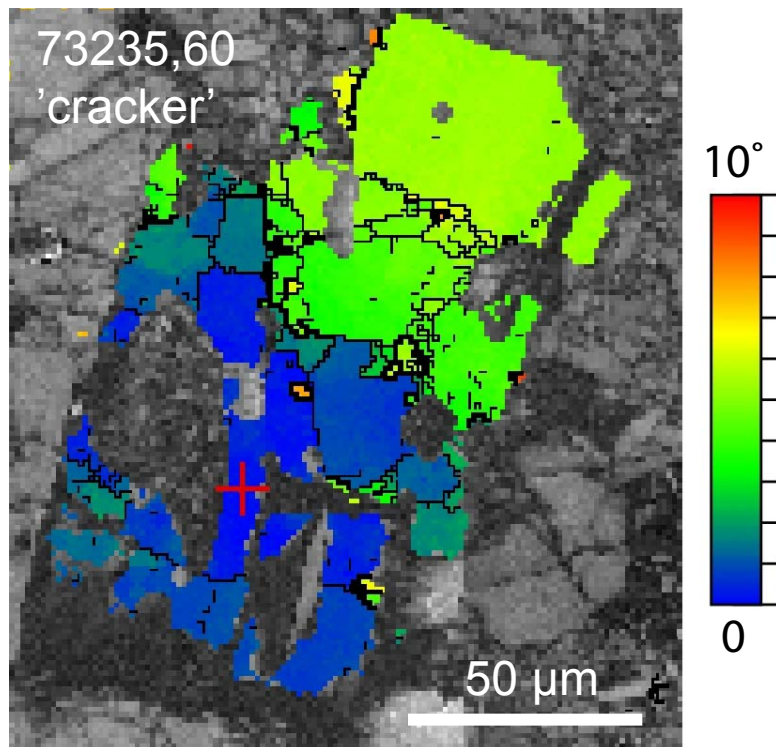


**Figure 13**

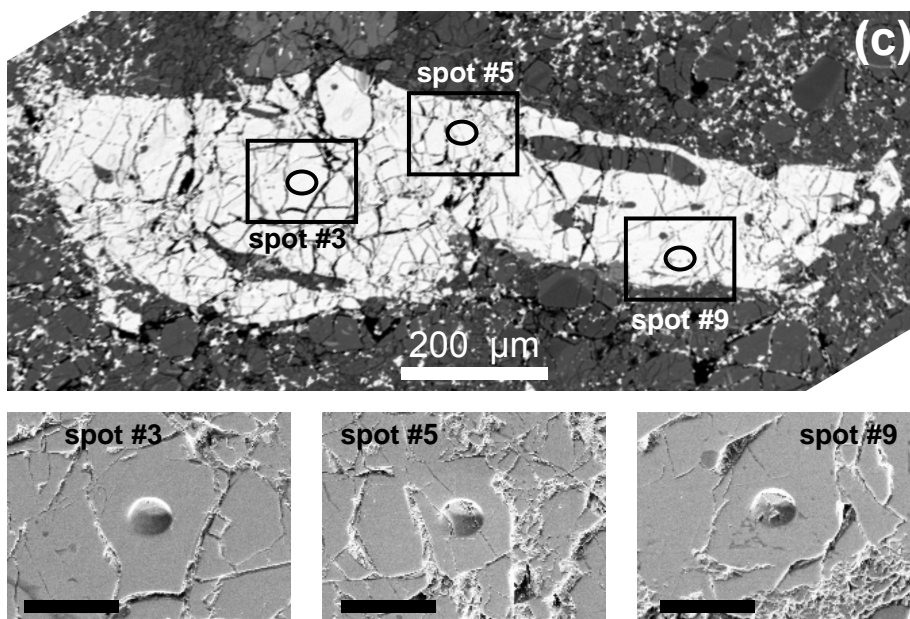
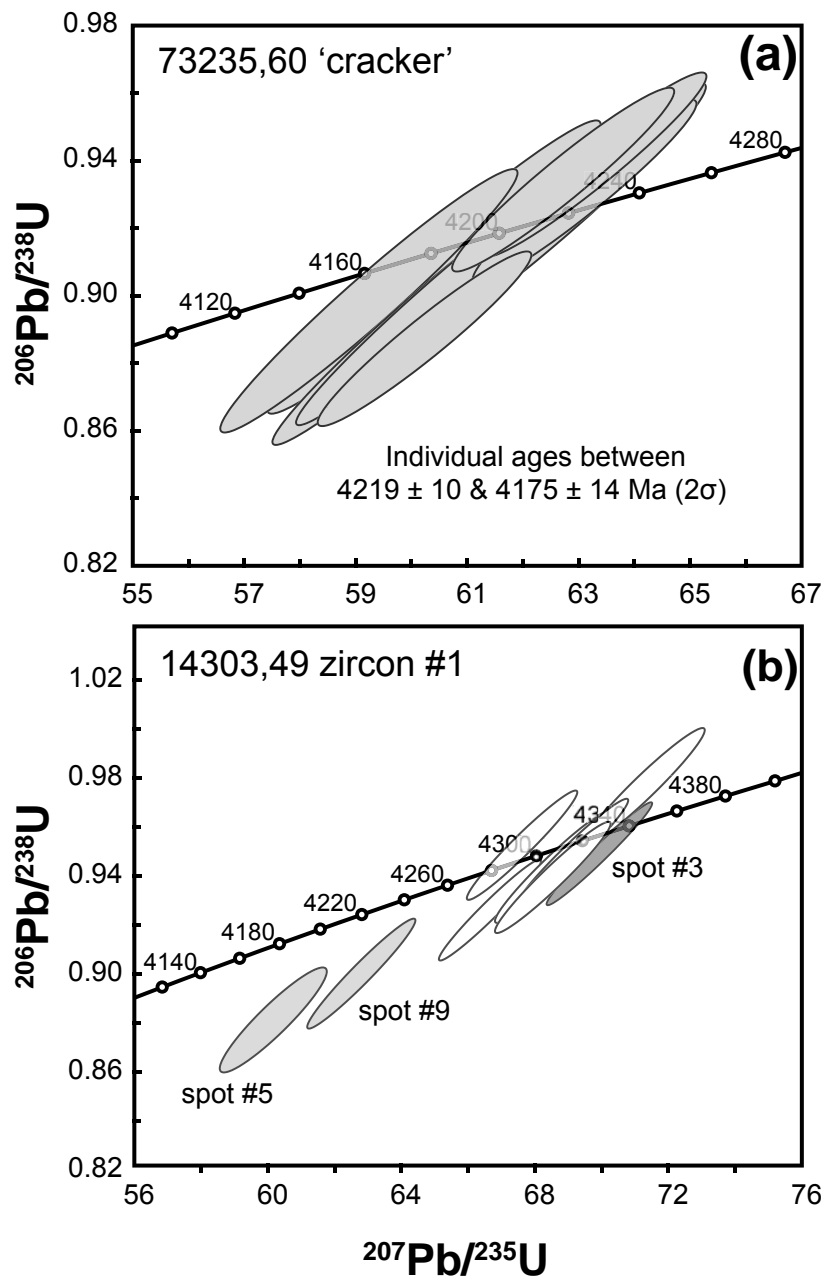


**Figure 14**

Primary Growth Events

Secondary Features

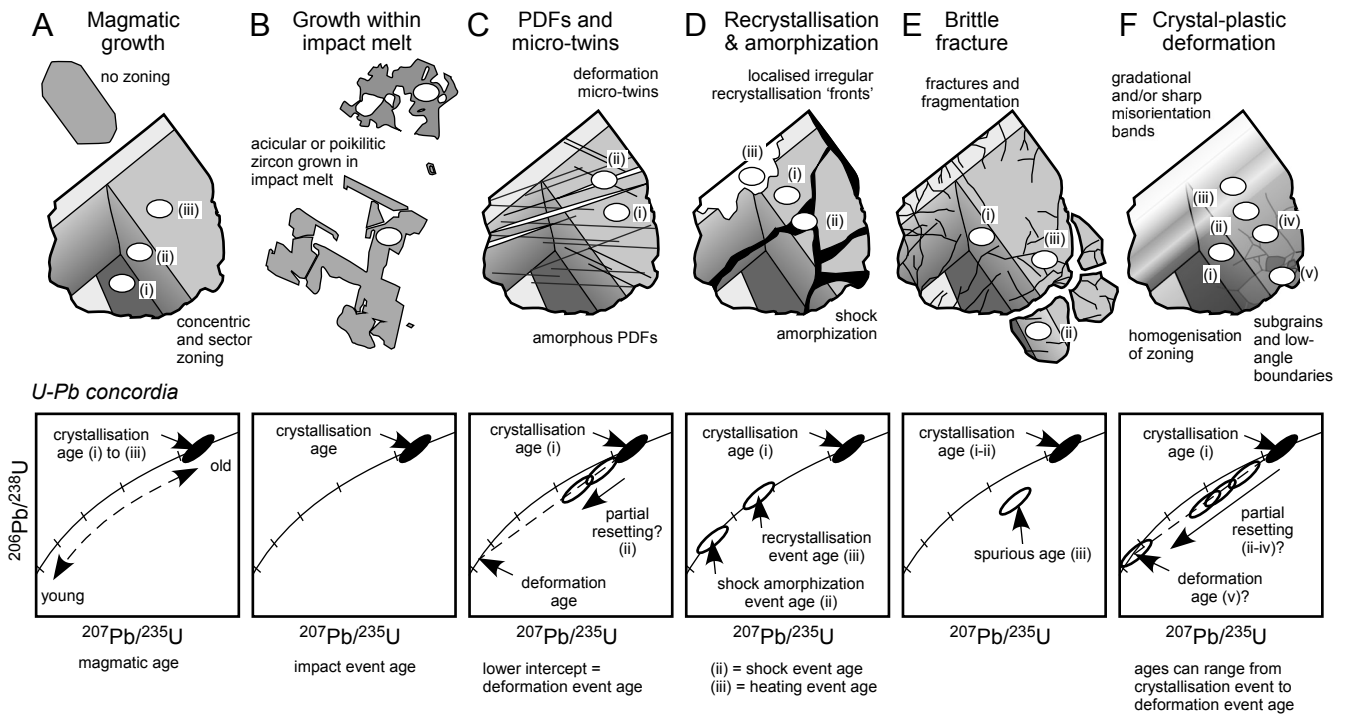


Figure 15